frontiers | Frontiers in Chemistry

TYPE Original Research
PUBLISHED 04 January 2023
DOI 10.3389/fchem.2022.1102920

OPEN ACCESS

EDITED BY
Chiara Cappelli,
Scuola Normale Superiore, Italy

REVIEWED BY
Jiani Qin,
Shaanxi University of Science and Technology, China
Feng-Ming Zhang,
Harbin University of Science and Technology, China

*CORRESPONDENCE
Ayman H. Zaki,
ayman.zaki@psas.bsu.edu.eg

SPECIALTY SECTION
This article was submitted to Nanoscience, a section of the journal Frontiers in Chemistry

RECEIVED 19 November 2022
ACCEPTED 12 December 2022
PUBLISHED 04 January 2023

CITATION
Abdel Aziz YS, Sanad MMS, Abdelhameed RM and Zaki AH (2023), *In-situ* construction of Zr-based metal-organic framework core-shell heterostructure for photocatalytic degradation of organic pollutants. *Front. Chem.* 10:1102920. doi: 10.3389/fchem.2022.1102920

In-situ construction of Zr-based metal-organic framework core-shell heterostructure for photocatalytic degradation of organic pollutants

Yasmeen S. Abdel Aziz[1], Moustafa M. S. Sanad[2], Reda M. Abdelhameed[3] and Ayman H. Zaki[4,5]*

[1]National Institute of Oceanography and Fisheries (NIOF), Cairo, Egypt, [2]Central Metallurgical Research and Development Institute, (CMRDI), Cairo, Egypt, [3]Applied Organic Chemistry Department, Chemical Industries Research Institute, National Research Centre, Giza, Egypt, [4]Materials Science and Nanotechnology Department, Faculty of Postgraduate Studies for Advanced Sciences, Beni-Suef University, Beni Suef, Egypt, [5]International Center for Materials Nanoarchitechtonics (WPI-MANA), National Institute for Materials Science, Tsukuba, Japan

Photocatalysis is an eco-friendly promising approach to the degradation of textile dyes. The majority of reported studies involved remediation of dyes with an initial concentration ≤50 mg/L, which was away from the existing values in textile wastewater. Herein, a simple solvothermal route was utilized to synthesize $CoFe_2O_4$@UiO-66 core-shell heterojunction photocatalyst for the first time. The photocatalytic performance of the as-synthesized catalysts was assessed through the photodegradation of methylene blue (MB) and methyl orange (MO) dyes at an initial concentration (100 mg/L). Under simulated solar irradiation, improved photocatalytic performance was accomplished by as-obtained $CoFe_2O_4$@UiO-66 heterojunction compared to bare UiO-66 and $CoFe_2O_4$. The overall removal efficiency of dyes (100 mg/L) over $CoFe_2O_4$@UiO-66 (50 mg/L) reached >60% within 180 min. The optical and photoelectrochemical measurements showed an enhanced visible light absorption capacity as well as effective interfacial charge separation and transfer over $CoFe_2O_4$@UiO-66, emphasizing the successful construction of heterojunction. The degradation mechanism was further explored, which revealed the contribution of holes (h^+), superoxide ($\bullet O_2^-$), and hydroxyl ($\bullet OH$) radicals in the degradation process, however, h^+ were the predominant reactive species. This work might open up new insights for designing MOF-based core-shell heterostructured photocatalysts for the remediation of industrial organic pollutants.

KEYWORDS

photocatalysis, MOFs, ferrite, core-shell, visible light, dyes

1 Introduction

Among various industrial sectors, the textile industry takes prominence due to the high utilization of water, raw materials, and chemicals including acids, chelating and bleaching agents, dyes, surfactants, *etc.* As a consequence, tremendous volumes of wastewater are released from this industry. It is estimated that 20% of global industrial wastewater emerges merely from textile industries (Holkar et al., 2016). In general, the textile effluent is characterized by high pH, intense color, high chemical and biochemical oxygen demands (COD and BOD5, respectively), and high concentrations of total suspended and dissolved solids (Yaseen and Scholz, 2019). Nevertheless, the composition of such effluents varies considerably in concentration and toxicity depending on the utilized chemicals, operating conditions, and the employed manufacturing steps (Ramos et al., 2021). Approximately 700,000 tons of synthetic dyes are produced annually and around 30% of this dyestuff ends up as industrial effluent (Al-Mamun et al., 2019). Owing to their complex aromatic structure and non-biodegradable nature, most of these dyes may present carcinogenic and/or mutagenic potentials to human health and aquatic ecosystem (Nidheesh et al., 2013; Dihom et al., 2022). Hence, efficient treatment of textile wastewater before discharge into water bodies has become of crucial importance.

Inspired by the natural photosynthesis process, photocatalysis has currently emerged as a promising green approach for the conversion of solar energy into chemical energy (Gao et al., 2017). Due to its high efficiency, feasibility, low energy consumption, and eco-friendly feature, semiconductor-induced photocatalysis has been successfully harnessed in diverse applications including energy storage and conversion (Wei et al., 2021; Han et al., 2022; Qin et al., 2022), CO_2 reduction (Li et al., 2020; Xiong et al., 2020), organic synthesis (Zhang et al., 2019b; Xiong and Tang, 2021), Cr(VI) reduction (Yi et al., 2019; Zhang et al., 2020) and water treatment (Zeng et al., 2018; Feng et al., 2022; Shi et al., 2022). Up to present, several semiconductor photocatalysts have been intensively studied such as metal oxides [TiO_2, ZnO, Fe_2O_3 (Ba-Abbad et al., 2013; Franking et al., 2013; Kreft et al., 2020)], metal sulphides [MoS_2, CdS, In_2S_4 (Ning et al., 2019; Liang et al., 2021; Pan et al., 2021)], and organic semiconductors [(g-C_3N_4, perylene diimide, covalent organic framework (Zhou et al., 2018; Sivula, 2020; Zhou et al., 2021)]. Nevertheless, the photocatalytic performance of these catalysts is far unsatisfactory owing to various limitations like photocorrosion, low photon absorption efficiency, inefficient charge separation, most importantly; deficiency of effective and stable catalytic sites to maintain dynamic photocatalytic reactions (Gao et al., 2017).

As a distinct group of organic-inorganic hybrid crystalline porous materials, metal-organic frameworks (MOFs) have shown considerable potential in a variety of applications involving adsorption, drug delivery, gas storage and separation, and catalysis (Lei et al., 2018; Wang et al., 2020a; Wang et al., 2020b; Connolly et al., 2020; Younes et al., 2022). Due to their distinguished features such as tunable pore structure, high specific surface area with abundant catalytic active sites, and adjustable electronic and optical properties, MOFs have recently perceived unparalleled progress in the field of photocatalysis (Qin et al., 2020; Xia et al., 2021). Unlike conventional photocatalysts, MOFs are characterized by a special charge transition mechanism, where, the electronic states are localized, reducing the transmission distance of photoinduced carriers (Liang et al., 2019; Zhang et al., 2021c). Upon light illumination, the organic linkers, as light-absorbing antennas, and metal clusters, as semiconductor quantum dots, are excited to generate electron-hole pairs (Dey and Gogate, 2021). Consequently, several photo-excitation pathways are proposed to explore the photon harvesting process in MOF-based photocatalysts such as metal-to-ligand charge transfer (MLCT), metal-to-metal-to-ligand charge transfer (MMLCT), ligand-to-metal charge transfer (LMCT), and ligand-to-ligand charge transfer (LLCT) (Wen et al., 2019).

Beyond other reported MOF's, zirconium Zr(IV)-based MOFs (e.g. UiO-66), have drawn tremendous interest because of their superb thermal and chemical stability even in acidic and some basic mediums, which is mostly attributed to the robust interaction between Zr-O clusters and carboxylate ligands (Yuan et al., 2018; Yuan et al., 2021). Hence, Zr-MOFs have emerged as an exciting class for photocatalytic potential applications in an aqueous environment (Zhang et al., 2021d; Zhang et al., 2021c). However, the photocatalytic performance of UiO-66(Zr) still does not reach the utmost level due to its relatively wide bandgap energy (~3.8 eV). Thus, UiO-66 can only absorb light in the ultraviolet region (3–4%), leaving more than 90% of the solar spectrum unutilized. This in turn, results in a low photoconversion efficiency and limits the practical application of UiO-66 photocatalyst for solar light harvesting (Cheng et al., 2016; Gao et al., 2017). To fulfill the sustainable development concepts, several approaches have been embraced for promoting the photocatalytic efficiency of UiO-66(Zr) including bandgap engineering (Taddei et al., 2019), element doping (Qiu et al., 2019), ligand functionalization (Wang et al., 2021c), active site regulation (Shen et al., 2015b), *etc.* Interestingly, the construction of heterojunction structures has been reported as one of the most prospective strategies to boost the photocatalytic performance of Zr-MOFs through the formation of an interface between the two semiconductors (Subudhi et al., 2020; Zhang et al., 2021b). This intimate interfacial contact, in turn, favors accelerated charge transfer and boosts solar energy exploitation by modulating the band gap energy to attain the utmost photocatalytic efficiency (Jabbar and Graimed, 2022).

For example, Zhang et al. adopted facile adsorption and thermal conversion technique to encapsulate the α-Fe_2O_3 nanoclusters inside UiO-66 cavities for the construction of a

visible light-driven α-Fe_2O_3@UiO-66 photocatalyst heterostructure for catalytic degradation of MB (Zhang et al., 2019a). Under visible light excitation, Fe_2O_3@UiO-66 displayed considerably boosted degradation performance. This prominent improvement of photoactivity of Fe_2O_3@UiO-66 could be explained by the synergetic interaction between UiO-66 and α-Fe_2O_3, which is beneficial to enhancing charge migration and lowering the recombination rate. Similarly, Yassin et al. prepared Ag_3PO_4/Zr-BDC/g-C_3N_4 ternary heterostructure for discoloration of MB under visible and solar irradiations (Yassin et al., 2022). Noteworthy, the UiO-66 bandgap energy is modulated from 3.72 eV to 2.91 eV in the Ag_3PO_4/Zr-BDC/g-C_3N_4 heterojunction, interpreting the effective absorption toward the visible spectrum. In comparison with pristine materials, Ag_3PO_4/Zr-BDC/g-C_3N_4 showed remarkably high degradation efficiency (95.0%) within 240 min under visible illumination, which might be credited to the spatial charge separation and prolonged carrier lifetime, confirmed by the significantly suppressed intensity of photoluminescence (PL) emission spectra. In addition, although numerous reports have revealed the splendid catalytic activity of Zr-MOF/metal oxide heterostructures for wastewater treatment, the high cost of some metal nanoparticles (e.g. noble metals), metal-ion leaching, and instability often restrict their practical applications (Zhang et al., 2021d; Mukherjee et al., 2022).

At present, cobalt ferrite ($CoFe_2O_4$), a spinel-type ferrite, has displayed marked potential as a versatile photocatalyst due to its facile synthesis, low cost, excellent magnetic anisotropy, high chemical stability, and narrow bandgap energy (~2.0 eV) with visible light absorption capacity (Mathew and Juang, 2007; Mmelesi et al., 2021). In a recent study, it has been reported complete degradation of ciprofloxacin within 45 min of visible-light irradiation by $CoFe_2O_4$/ZnO nanoheterojunction (Shawky and Alshaikh, 2022). The excellent photocatalytic activity of the composite is explicated by the notable decline in the bandgap after the incorporation of $CoFe_2O_4$ as well as the inhibition of charge-transport resistance through the formed p-n nanoheterojunction. In another study, Khosroshahi et al. designed a novel magnetic $CoFe_2O_4$/Ce-UiO-66 nanocomposite through a self-assembly approach for photocatalytic oxidation of aliphatic alcohols. Upon visible irradiation, the embedded composite demonstrated superior performance for selective oxidation of alcohols with a conversion ratio of 75%–90% compared to 21% and 10% conversion for $CoFe_2O_4$ and Ce-UiO-66, respectively (Khosroshahi et al., 2021). Despite the fact that the magnetic behavior of $CoFe_2O_4$ has been extensively investigated, studies on its optical and photoelectrochemical properties are still in infancy, particularly, with concerns for poor efficiency owing to the swift recombination of carriers under light irradiation and its relatively low specific surface area (Kefeni and Mamba, 2020; Görmez et al., 2022). Based on that, the construction of core-shell Zr-MOF-based composites has been recognized as an attractive approach to effectively promote photostability and enlarge the specific surface area, which is conducive to exposing more active sites in the photocatalytic reaction (Liu et al., 2021).

In this report, we successfully prepared a novel $CoFe_2O_4$@UiO-66 core-shell heterostructure photocatalyst *via* a simple solvothermal route for photodegradation of textile MB and MO dyes under simulated solar irradiation. Even though the initial concentration of dyes in actual textile wastewater samples has been recorded as higher than 100 mg/L, the majority of reported studies involved dye removal with an initial concentration of less than 50 mg/L (Mukherjee et al., 2022). Thus, dyes of 100 mg/L as an initial concentration were used in this study to provide realistic conditions similar to that in real textile wastewater. The crystallinity, surface composition, morphology, porosity, thermal stability, and optical and photo electrochemical properties of the prepared catalysts were investigated in detail. In addition, radical quenching experiments were applied to explore the possible photocatalytic mechanism.

2 Experimental

2.1 Materials

Zirconyl chloride ($ZrOCl_2.8H_2O$, 99%), 1,4-benzenedicarboxylic acid (H_2BDC) ($C_8H_6O_4$, 98%), and benzoquinone (*p*-BQ) ($C_6H_4O_2$, ≥98%) were purchased from Sigma-Aldrich cooperation. Ethylenediaminetetraacetic acid disodium salt (EDTA-2Na, $C_{10}H_{14}N_2Na_2O_8$. H_2O) and ammonium hydroxide (NH_4OH) were supplied by BioChem Chemopharma Co. *N,N*-dimethylformamide (DMF, 99.5%), acetic acid (CH_3COOH, ≥99%), and ethanol (C_2H_6O, ≥99.8%) were acquired from Carlo Erba Reagent Co, Ltd. 2-propanol (C_3H_8O, 99.7%) was provided by Merck. Methylene blue (MB, $C_{16}H_{18}ClN_3S$) and methyl orange (MO, $C_{14}H_{14}N_3NaO_3S$) were supplied by LOBA Chemie Pvt. Ltd. Ferric chloride ($FeCl_3$), cobalt (II) chloride hexahydrate ($CoCl_2.6H_2O$) were purchased from Oxford Lab Reagents Co. All reagents were of analytical grade and utilized without further purification. Deionized water was applied in the following experiments.

2.2 Preparation of photocatalysts

2.2.1 Synthesis of $CoFe_2O_4$

$CoFe_2O_4$ nanoparticles were prepared by the co-precipitation method (Esmat et al., 2017). Briefly, 2.0 mol of $FeCl_3$ and 1.0 mol of $CoCl_2.6H_2O$ were dispersed into 30 ml of deionized water. Following that, NH_4OH (1.0 M) was added dropwise until the pH reaches 10 and then left for complete precipitation. Afterward, the precipitate was collected *via* filtration, followed by washing it with deionized water. Subsequently, the precipitate

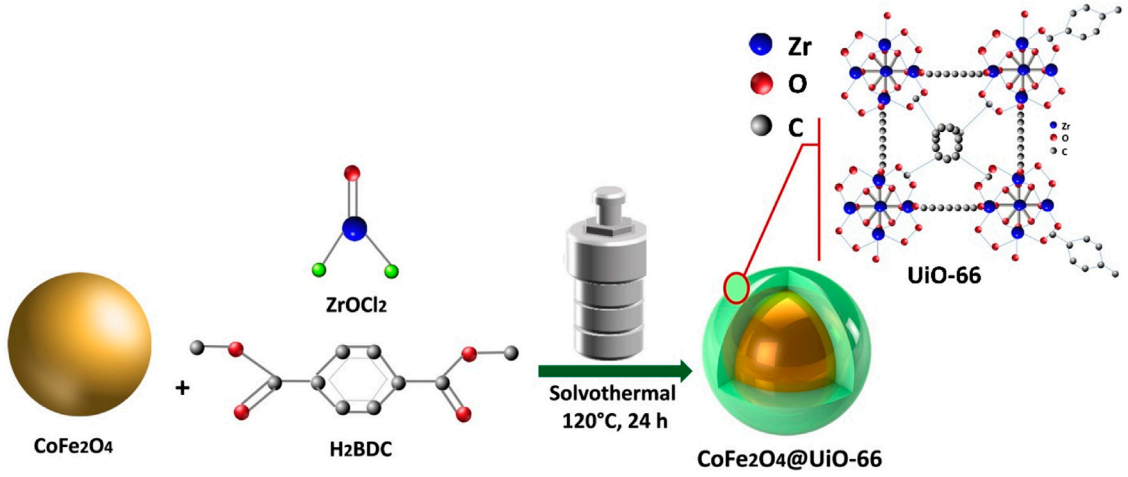

SCHEME 1
Schematic representation of $CoFe_2O_4$@UiO-66 composite preparation.

was air-dried at 100°C in a drying chamber. Lastly, the dried powder was calcined in a muffle furnace for 2 h at 500°C to get $CoFe_2O_4$ nanoparticles.

2.2.2 Synthesis of UiO-66

UiO-66 octahedrons were prepared through a modified scale-up procedure. Initially, 3.75 g of $ZrOCl_2$ and 3.7 g of H_2BDC were dispersed in 450 ml of DMF using ultrasonication for 60 min. Then, 20 ml of acetic acid was subsequently added to the mixture as a modulator to regulate the morphology of UiO-66. Next, the solution was poured into a 1,000 ml Teflon-lined stainless-steel reactor and heated for 24 h at 120°C. After cooling down, the white precipitate was obtained *via* filtration and washed meticulously several times with DMF and ethanol, respectively, to ensure the removal of any residual reactant. Finally, the UiO-66 nanoparticles were vacuum-dried for 12 h at 85°C.

2.2.3 Synthesis of $CoFe_2O_4$@UiO-66 composite

As illustrated in Scheme 1, a facile solvothermal method was adapted to prepare $CoFe_2O_4$@UiO-66 core-shell composite. Typically, 1.0 g of $CoFe_2O_4$ was dissolved in 450 ml DMF solution. Simultaneously, 3.75 g of $ZrOCl_2$ and 3.7 g of H_2BDC were dispersed in 20 ml of acetic acid. The prepared solutions were then mixed by ultrasonication for 60 min. Afterward, the homogenous solution was poured into a 1,000 ml Teflon-lined stainless-steel reactor and heated for 24 h at 120°C. After cooling down, the brown composite was separated and washed following the aforementioned washing process of UiO-66. In the end, the as-prepared product was vacuum-dried for 12 h at 85°C.

2.3 Characterization

The X-ray diffraction (XRD) patterns were recorded using an XRD diffractometer (PANalytical Empyrean, Switzerland) with Cu-Kα (ʎ = 1.5405 Å) radiation source, operating at a voltage and current of 30 mA and 40 kV, respectively. The morphology and microstructure characteristics of the as-fabricated materials were studied using a field emission scanning electron microscope equipped with an energy-dispersive spectrometer (EDS) system (FE-SEM, Zeiss Sigma 500 VP, Germany) and transmission electron microscope (TEM, JEOL JEM-2100F, Japan). Fourier transform infrared (FTIR) spectra were measured using a VERTEX 70 spectrophotometer (Bruker Optics, Germany). X-ray photoelectron spectroscopy (XPS) with Al-Kα radiation (Thermo ESCALAB 250XI, United State) was applied to examine the oxidation state of the prepared composite. N_2 adsorption-desorption analysis was performed on BELSORP-MAX II surface area analyzer (MICROTRAC, Germany) at 77 K. Brunauer-Emmett-Teller (BET) and Barrett- Joyner-Halenda (BJH) methods were utilized to calculate the specific surface area and pore size distribution. Prior to measurement, the samples were vacuum-activated for 12 h at 150°C and then degassed for 3 h at 120°C. Thermogravimetric analysis (TGA) was conducted employing a LabSys EVO thermogravimetric analyzer (SETARAM, France) from room temperature to 800 °C under N_2 atmosphere with a 10°C/min heating rate. The surface charge was measured on a Zeta potential analyzer (Zetasizer Nano ZS, Malvern, United Kingdom). The UV–visible diffuse reflectance spectra (UV–vis DRS) were determined using a UV–Vis spectrophotometer (Jasco V-770, Japan) with $BaSO_4$ as a

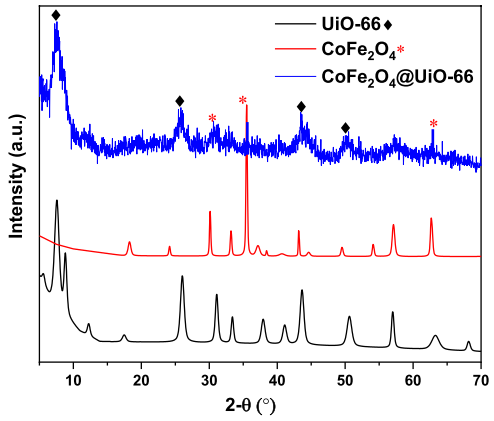

FIGURE 1
XRD patterns of UiO-66, $CoFe_2O_4$, and $CoFe_2O_4$@UiO-66 composite.

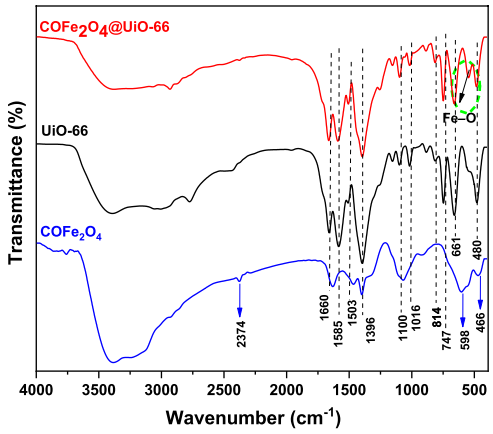

FIGURE 2
FTIR spectra of UiO-66, $CoFe_2O_4$, and $CoFe_2O_4$@UiO-66 composite.

reference in the spectral range of 200–800 nm. The photoluminescence (PL) spectra were obtained by a fluorescence spectrometer (Jasco FP-6500, Japan) with an excitation wavelength of 320 nm for $CoFe_2O_4$ and 297 nm for UiO-66 and $CoFe_2O_4$@UiO-66.

2.4 Photoelectrochemical measurements

The photoelectrochemical characterization of the as-prepared catalysts was analyzed using a standard three-electrode electrochemical workstation system (Parastat 4,000 Princeton, United State) equipped with a Xenon lamp (150 W) as an irradiation source. Indium-tin-oxide (ITO) glass coated by the catalysts ($\rho \sim 30\ \Omega/cm^2$) served as the working electrode against the Pt sheet and saturated Ag/AgCl as the counter and reference electrodes, respectively. 0.1 M Na_2SO_4 was adopted as the electrolyte solution. The Mott-Schottky plots were estimated with the same electrochemical instrument at 500 Hz frequency under dark conditions. The electrochemical impedance spectroscopy (EIS) was recorded over a frequency range of 1 MHz–10 mHz with an amplitude of 50 mV at an open-circuit potential. Linear sweep voltammetry (LSV) tests were performed by sweeping the potential from 0 to 1.0 V.

2.5 Photocatalytic reaction

The photocatalytic performance of UiO-66, $CoFe_2O_4$, and $CoFe_2O_4$@UiO-66 composite was assessed through the photodegradation of MB and MO dyes. The physicochemical properties of the former dyes are presented in Supplementary Table S1. In a typical procedure, 50 mg of catalysts were added to 25 mL of each dye solution (100 mg/L). After agitation for 60 min in dark to establish adsorption-desorption equilibrium, the solutions were irradiated by Solar Simulator (Oriel®Sol1A, Newport Co.) equipped with a 150 W xenon lamp (100 mW/cm^2 light intensity). At regular time intervals, 100 µL of the sample solution was extracted, diluted to 700 µL with deionized water, and then centrifuged to separate the residual photocatalyst. The concentration of MB and MO was calibrated using a UV–vis spectrophotometer (UV-2600, Shimadzu, Japan) at maximum absorption wavelength (λ_{max}) of 664 nm and 464 nm, respectively. The removal efficiency (%) was calculated following Eq. 1

$$\text{Removal efficiency } (\%) = \frac{C0 - Ct}{C0} \times 100 \quad (1)$$

where C_0 and C_t (mg/L) are the dye concentration at initial and each interval time, respectively.

To investigate the photocatalytic mechanism, disodium ethylenediaminetetraacetic acid (EDTA-2Na), *p*-benzoquinone (BQ), and isopropanol (IPA) were used as trapping agents for photogenerated holes (h^+), superoxide radicals ($\bullet O_2^-$) and hydroxyl radicals (•OH), respectively. The concentration of the scavengers was set as 2 m and the photocatalytic assays were carried out following the same procedure described above under the same pH.

3 Results and discussions

3.1 Photocatalysts characterization

3.1.1 Structure analysis

The crystallinity of the as-prepared samples was examined using XRD analysis. The simulated patterns of

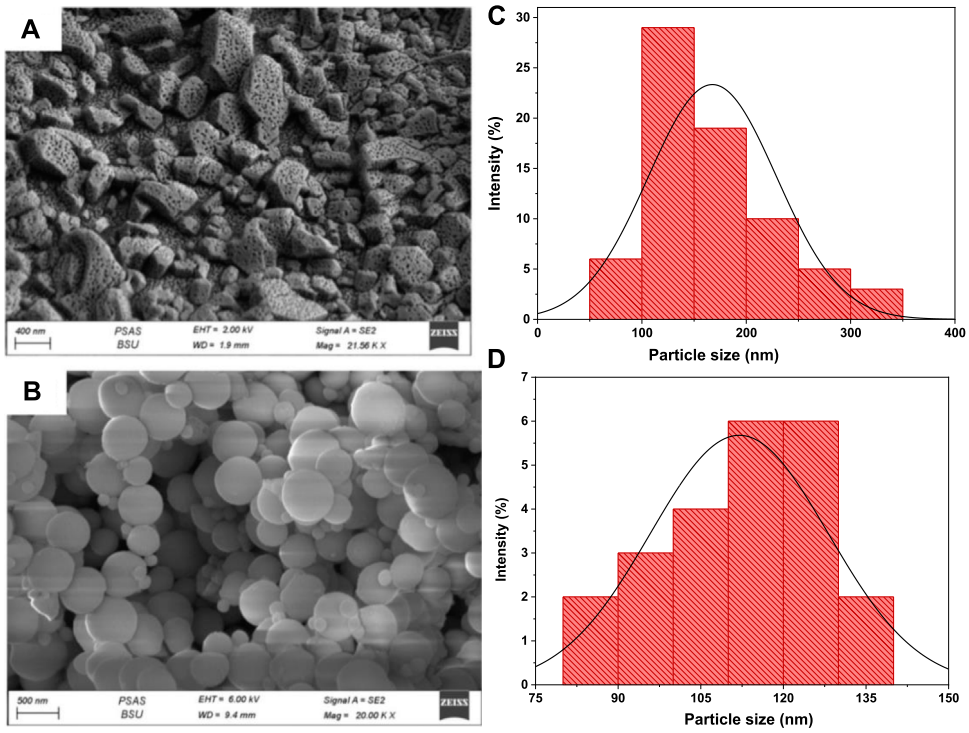

FIGURE 3
FESEM images of UiO-66 **(A)** and $CoFe_2O_4$@UiO-66 composite **(B)**; UiO-66 particle size distribution of UiO-66 **(C)** and $CoFe_2O_4$@UiO-66 composite **(D)**.

UiO-66 and $CoFe_2O_4$ are presented in Supplementary Figure S1. From Figure 1, it can be seen that the as-synthesized UiO-66 exhibited typical characteristic peaks cited at 7.5°, 8.6° indexed to the (111) and (200) crystal planes, respectively. Moreover, distinct peaks appeared at values of 12.21°, 17.4°, 25.9°, 31.0°, 33.4°, 37.7, 40.9°, 43.7°, 50.5°, and 57.1° agreed with (220), (400), (600), (711), (731), (751), (664), (933), (955), and (1242) crystal planes of UiO-66, respectively. This observation is in agreement with the former studies (Zhang et al., 2019c; Mirhosseini-Eshkevari et al., 2019; Gao et al., 2021), implying the successful preparation of the obtained material. Meanwhile, $CoFe_2O_4$ showed diffraction peaks at 18.27° (111), 30.21° (220), 35.51° (311), 43.32° (400), 53.9° (422), 57.14° (411), and 62.79° (440), which are consistent with the standard peak positions of spinel $CoFe_2O_4$ structure (Jia et al., 2019). For the $CoFe_2O_4$@UiO-66 heterojunction, the diffraction peaks correlating to UiO-66 appeared with a relative broadening and fluctuations of peak intensities, is indicative of a little alternation in the framework structural regularity (Bi et al., 2020). Even though the $CoFe_2O_4$ characteristic peaks noticeably weakened in the heterojunction owing to the *in-situ* growth of the UiO-66 shell, they still could be distinguished. Given this, the aforementioned findings suggest the successful fabrication of the MOF-hybrid material.

FTIR spectroscopy was implemented to investigate the surface functionalization of the as-prepared samples. Figure 2 displays the FTIR spectra of UiO-66, $CoFe_2O_4$, and $CoFe_2O_4$@UiO-66 composite. All samples showed a broad band at 3,200–3,500 cm^{-1} related to the O–H stretching vibration of absorbed water molecules (Ding et al., 2017; Basak et al., 2021). For UiO-66, typical bands can be identified at 1,585 and 1,396 cm^{-1}, corresponding to O–C–O asymmetric and symmetric vibrations of the -COOH group of the BDC ligand, respectively (Liu et al., 2018). The weak vibrational bands at 1,503 and 1,660 cm^{-1} occurred by the C=C vibration of benzene ring (Shangkum et al., 2018) and the C=O carbonyl stretching in the BDC linker (Ebrahim and Bandosz, 2013), respectively. Meanwhile, the bands sited around 1,016 and 1,100 cm^{-1} are ascribed to the Zr–O stretching vibration of the framework (Chen et al., 2017; Bariki et al., 2020). At lower frequency, the peaks appeared at 814, 747, and 661 cm^{-1} are associated with the O–H and C–H vibrations in the ligand (Ivanchikova et al., 2014). In addition, a distinct peak occurred at 480 cm^{-1} is assigned to asymmetric stretching of Zr-(OC) (Wang et al., 2021a). Concerning $CoFe_2O_4$, two characteristic peaks are

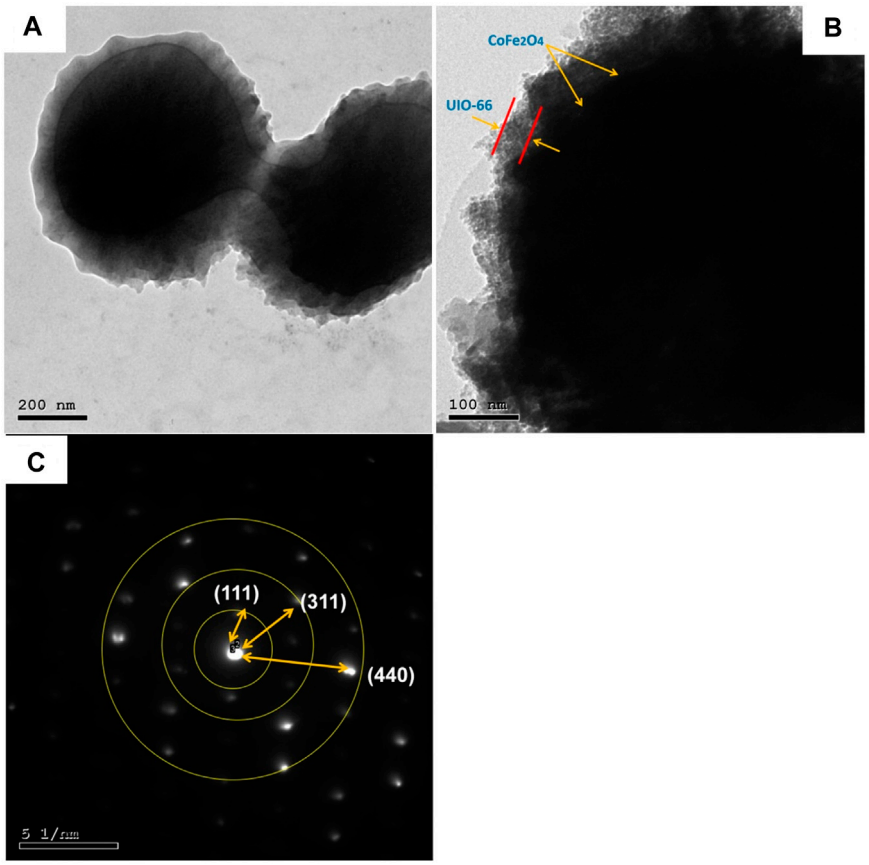

FIGURE 4
TEM images **(A,B)** and SAED pattern **(C)** of $CoFe_2O_4$@UiO-66 composite.

observed at 466 and 598 cm^{-1}, which are related to the metal-oxygen stretching vibrations at the octahedral and tetrahedral sites in the spinel structure, respectively (Shahjuee et al., 2017). The other peaks at 1,065, 1,392, and 1,629 cm^{-1} are appeared by O–H, C–O, and C–H bending vibration, respectively (Yavari et al., 2016). Meanwhile, a weak band noted at 2,374 cm^{-1} might be resulted from C–H stretching vibration (Johnson et al., 2020). As for $CoFe_2O_4$@UiO-66, the characteristic spectral bands of UiO-66 can be observed, nevertheless, with less intensity and slight blue-shift, indicating the changing of the chemical environment around UiO-66 following the incorporation of $CoFe_2O_4$. Unlike UiO-66, a new peak can be identified around 500–600 cm^{-1} in the composite material that is associated with the stretching vibration of Fe–O band (Deng et al., 2013). This observation confirms the effective integration of UiO-66 and $CoFe_2O_4$ to form the composite material, which corresponds with the above XRD findings.

3.1.2 Morphology analysis

FESEM analysis was adopted to explore the morphological characteristics of bare UiO-66 and CoFe2O4@UiO-66 composite. As displayed in Figure 3A, UiO-66 exhibited irregular cubic morphology with an average diameter approaching between 150–200 nm (Figure 3C). In fact, with increasing the concentration of monocarboxylic acid modulators, more comparatively uniform pores are created in the MOF network (Wang et al., 2021b). This explains the porous surface of the as-synthesized UiO-66, which could be resulting from the high concentration of acetic acid modulator utilized during the preparation process. Figure 3B shows the FESEM image of the $CoFe_2O_4$@UiO-66 composite. It is interestingly noted that after coating with UiO-66, $CoFe_2O_4$ maintained the original spherical-like structure previously reported (Mu et al., 2021), with a relatively uniform size and rough surface. On the other hand, the crystal size of UiO-66 has reduced to ~120 nm in the composite (Figure 3D), along with a morphological change from cubic to sphere-like crystals owing to the fast reaction between Zr and ligand (Han et al., 2017; Winarta et al., 2019).

TEM study was further carried out to explore the microstructure of the as-synthesized composite. As presented in Figures 4A, B, $CoFe_2O_4$@UiO-66 displayed a distinct core-shell structure comprised of $CoFe_2O_4$ core with an average diameter of approximately 550 nm,

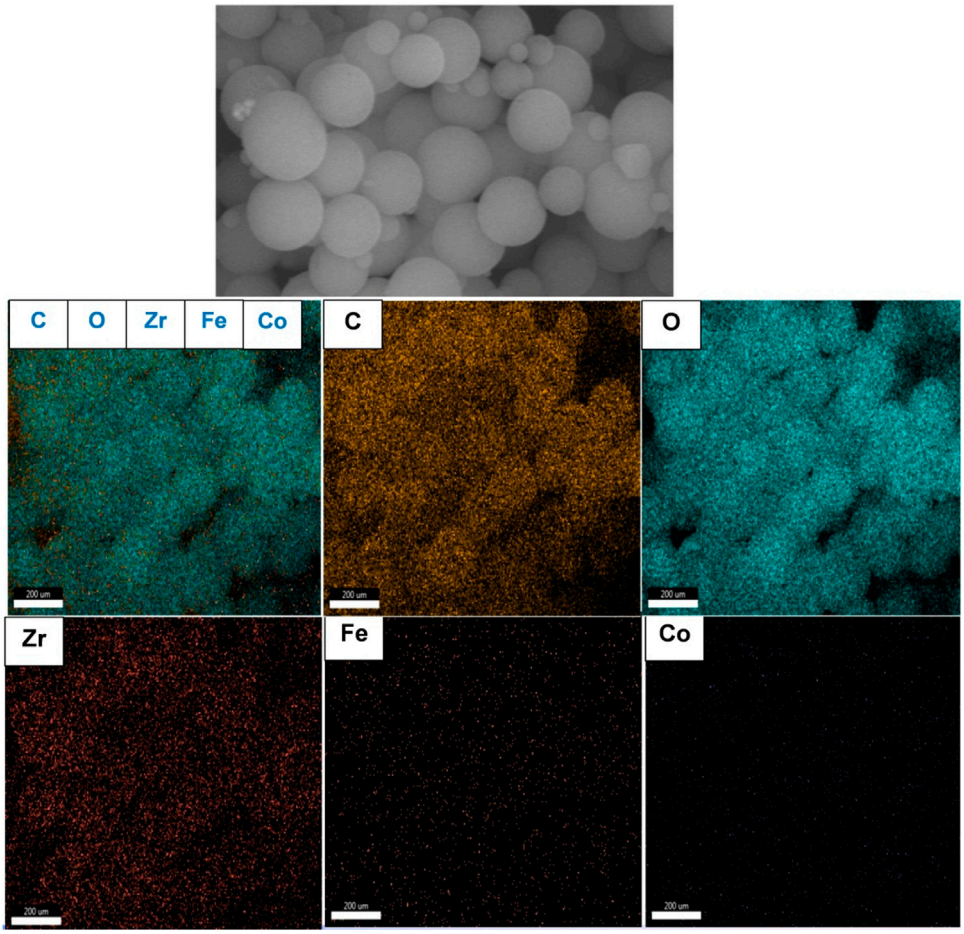

FIGURE 5
SEM-EDS elemental mapping of $CoFe_2O_4$@UiO-66 composite.

coated by an outer UiO-66 shell with a thickness of 42.4 ± 11.9 nm. Importantly, an obvious contact interface between UiO-66 and $CoFe_2O_4$ can be seen that accelerates the migration of charge carriers, thereby enhancing the photocatalytic performance. The selected area electron diffraction (SAED) pattern of the $CoFe_2O_4$@UiO-66 composite (Figure 4C) demonstrated the polycrystalline nature with d-spacing of 0.49, 0.26, and 0.15 nm correlated to (111), (311), and (440) planes of the magnetic $CoFe_2O_4$. The EDS elemental mapping of the $CoFe_2O_4$@UiO-66 composite is illustrated in Figure 5. Homogeneous distribution of Zr, O, C, Fe, and Co elements can be observed. This low content for Fe and Co elements might be ascribed to the entire coating of UiO-66 on $CoFe_2O_4$ microspheres. In addition, the photograph of different samples further proved that pristine and composite materials were successfully fabricated (Supplementry Figure S2).

3.1.3 XPS analysis

To explore the surface chemical state of the $CoFe_2O_4$@UiO-66 composite, the XPS spectra were recorded (Pan et al., 2022). The survey spectrum (Figure 6A) showed characteristic peaks for Zr 3d, Fe 2p, Co 2p, C 1s, and O 1s, accompanying intense peaks for the C and O elements corresponding to their relative abundance. For the C 1s spectrum (Figure 6B), three peaks at 284.5, 286.1, and 288.4 eV are respectively ascribed to C=C of the benzene ring and carboxylate groups of the BDC linker in the UiO-66 framework (Cao et al., 2018). As shown in Figure 6C, the O 1s spectrum demonstrated three deconvolution peaks cited at 530.1, 531.5, and 532.6 eV associated with the metal-oxygen bond (Zr–O) bond, C=O of the BDC linker, and surface adsorbed hydroxyl group, respectively (Yang et al., 2019). In Zr 3d XPS (Figure 6D), the characteristic binding energies of Zr $3d_{5/2}$ (at 182.5 eV) and Zr $3d_{3/2}$ (at 184.6 and 185.6 eV) can be seen, belonging to Zr–O core level interactions (Subhan et al., 2021). The energy spectrum of Co 2p depicted in Figure 6E demonstrated a pair of fitting peaks at 780.8 and 785.8 eV associated with Co $2p_{3/2}$ and another peak cited at 795.2 eV (with a relatively strong shake-up satellite peak at 800.4 eV) related to Co $2p_{1/2,}$ confirming the existence of Co^{2+} oxidation

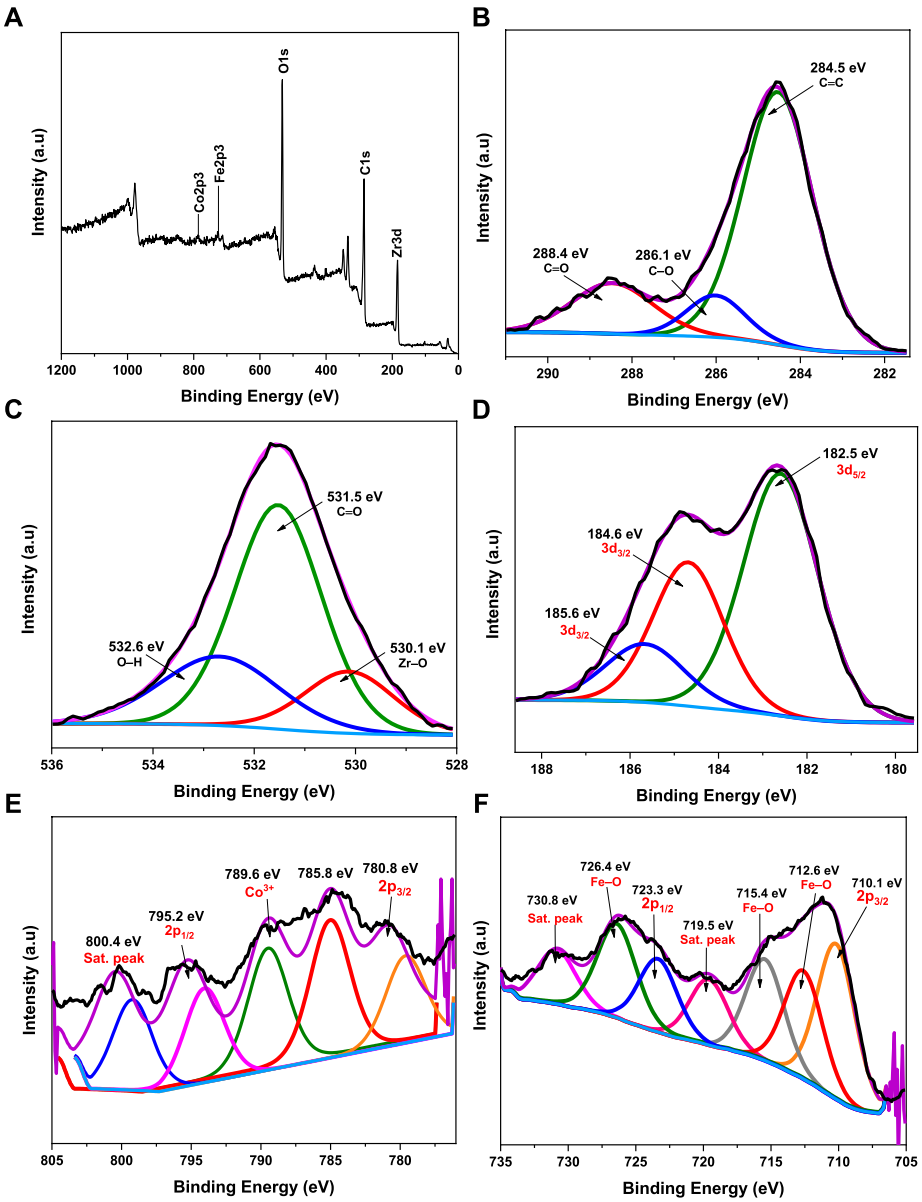

FIGURE 6
XPS spectra of $CoFe_2O_4$@UiO-66 composite: survey scan **(A)**, C 1s **(B)**, O 1s **(C)**, Zr 3 days **(D)**, Co 2p **(E)**, and Fe 2p **(F)**.

state in the spinal structure (Zhou et al., 2014; Chen et al., 2016). Typically, the satellite energy separation in oxides for Co^{3+} is approximately 8.5–9.5 eV (Xu et al., 2019). Given this, an extra peak centered at 789.6 eV corresponding to the binding energy of Co^{3+} $2p_{3/2}$ is presumably due to the surface oxidation of Co species after coating by UiO-66 particles. In the Fe 2p spectrum (Figure 6F), two distinct peaks located at 710.1 and 723.3 eV associated with the binding energies of Fe $2p_{3/2}$ and Fe $2p_{1/2}$, respectively, suggesting the existence of Fe^{2+} (Zhou et al., 2022), whereas, the Fe 2p shakeup satellites observed at 719.5 and 730.8 eV are assigned to Fe^{3+} spin state (Ma et al., 2015; Salunkhe et al., 2015). Moreover, the peaks noticed at 712.6, 715.4, and 726.4 eV could be due to Fe–O bonds, which further assert the strong interaction between $CoFe_2O_4$ and UiO-66 *via* Fe-O-Zr linkages (Xu et al., 2017).

3.1.4 Surface area and thermal investigation

N_2 adsorption-desorption isotherm studies were employed to investigate the textural properties of UiO-66 and $CoFe_2O_4$@UiO-66 composite and relevant data are given in Figure 7; Table 1. UiO-66 (Figure 7A) displayed type IV isotherm with a well-defined H2 hysteresis loop, indicating the existence of mesopores,

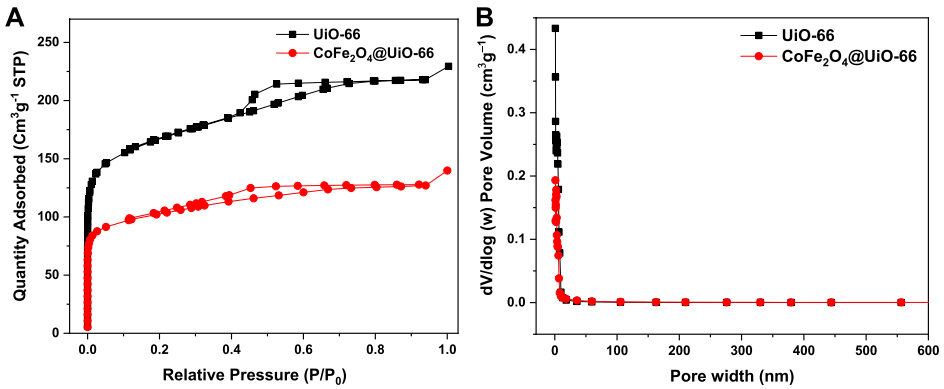

FIGURE 7
N_2 adsorption-desorption isotherms **(A)**, and pore size distribution curves **(B)** of UiO-66 and $CoFe_2O_4$@UiO-66 composite.

TABLE 1 Porous texture of the as-synthesized samples.

Sample	S_{BET} (m^2 g^{-1})[a]	$S_{Langmuir}$ (m^2 g^{-1})[b]	V_t (cm^3 g^{-1})[c]	Pore diameter (nm)[d]
UiO-66	593.94	742.31	0.35	2.36
$CoFe_2O_4$@UiO-66	375.7	480.03	0.21	2.27

[a]BET specific surface area.
[b]Langmuir specific surface area.
[c]Total pore volume measured at P/P_0 = .99.
[d]Pore size in diameter calculated by the desorption data using Barrett–Joyner–Halenda (BJH) method.

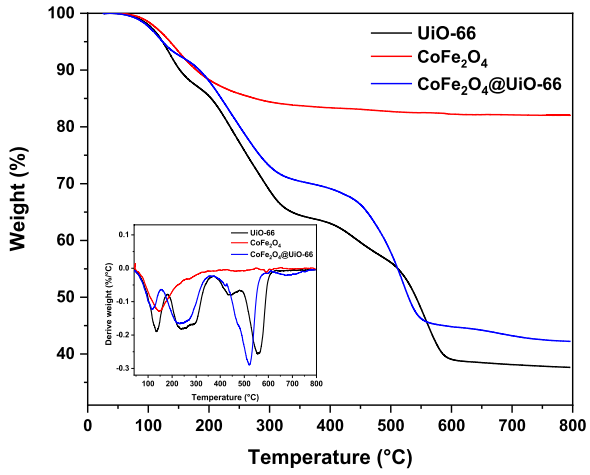

FIGURE 8
Thermal analysis of UiO-66, $CoFe_2O_4$, and $CoFe_2O_4$@UiO-66 composite, inset: the corresponding derivative thermogravimetric (DTG) plots.

thereby authenticating the results of FE-SEM. The S_{BET} of UiO-66 is 593.94 m^2 g^{-1}. Obviously, the $CoFe_2O_4$@UiO-66 composite attained the same isotherm pattern; however, with an H4 type hysteresis loop and S_{BET} of 375.7 m^2 g^{-1}. The pore size distribution of as-synthesized catalysts also showed a similar trend (Figure 7B), whereas, the total pore volumes for UiO-66 and $CoFe_2O_4$@UiO-66 are calculated to be 0.35 and 0.21 cm^3 g^{-1}, respectively. Distinctly, this reduction in the S_{BET} (~36%) and pore volume (~40%) of the composite material is possibly connected with the formation of larger mesopores owing to the encapsulation of $CoFe_2O_4$ particles into the MOF network (Lee et al., 2015; Qi et al., 2019).

To evaluate the thermal behavior of the as-prepared catalysts, TGA analysis was conducted and the findings are displayed in Figure 8. For $CoFe_2O_4$, two stages of weight loss with a total weight loss of ~16% can be observed. The major one occurred up to 100°C owing to the evaporation of moisture, whilst, the minor mass loss happened at 330°C could be assigned to the elimination of ammonium hydroxide and chloride from the surface (Chakhtouna et al., 2021). In contrast, no considerable weight loss can be detected above 330°C, revealing the high thermal stability of $CoFe_2O_4$. On the other side, both pristine and modified UiO-66 demonstrated similar TGA curves with three stages of weight loss. In the case of pristine UiO-66, an initial weight loss (13%) occurs from 33°C–161°C owing to the evaporation of physically adsorbed water molecules from the UiO-66 surface (Xu et al., 2022). In the second stage, nearly 19% weight loss observed in the range of 161°C–300°C is associated

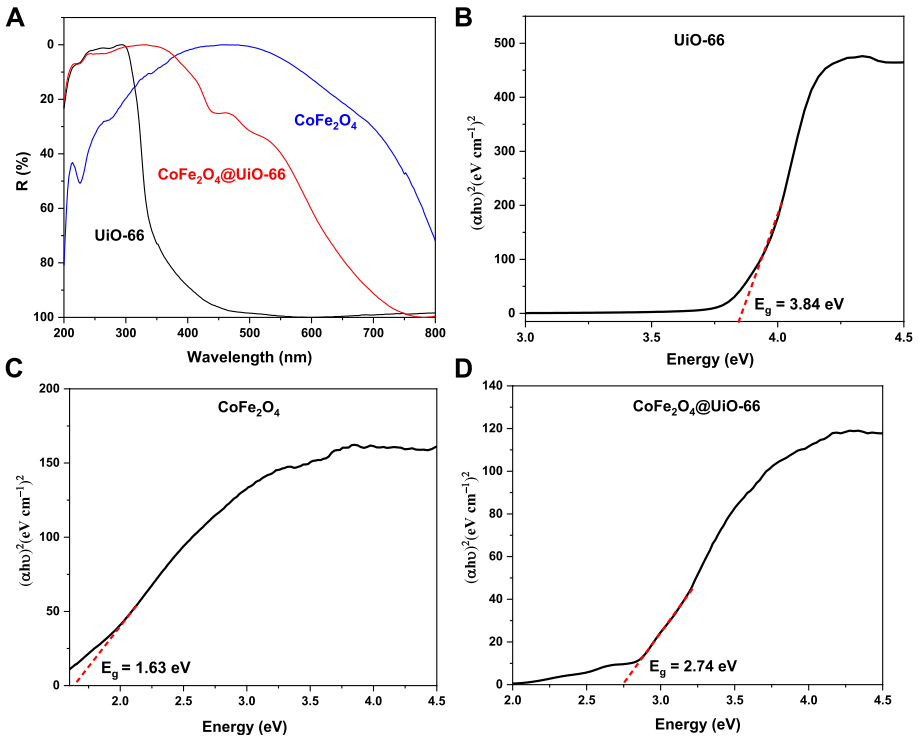

FIGURE 9
UV-vis DRS spectra **(A)**, bandgap (E_g) plots **(B–D)** of the as-synthesized samples.

with the removal of DMF molecules trapped inside the framework pores and thermal dehydration of zirconium clusters (Zhang et al., 2021a). The last weight loss (>30%) appeared at 430°C–600°C is ascribed to the thermal decomposition of the organic ligand to CO, CO_2, and ZrO_2 (Molavi et al., 2018). Compared to bare UiO-66, the TGA curve of $CoFe_2O_4$@UiO-66 showed a relative reduction in weight loss by about 6.22%, indicating an improvement of thermal stability after the introduction of $CoFe_2O_4$ nanoparticles.

3.2 Optical properties

The UV-Vis DRS was performed to study the photoabsorption characteristics of the as-synthesized photocatalysts and findings are shown in Figure 9A. It can be noticed that bare UiO-66 displayed no absorption in the visible region, however, strong absorption is obvious in the UV spectral region with an absorption peak at 296 nm that can be ascribed to Zr–Oxo-clusters (Wang et al., 2016). Otherwise, owing to the black color of pristine $CoFe_2O_4$, absorption peaks can be seen in both UV and visible regions (Jing et al., 2016). By comparison, the light absorption edge of $CoFe_2O_4$@UiO-66 composite is red-shifted to around 467 nm, evidencing the enhancement of light absorption intensity and visible light utilization efficiency after combining $CoFe_2O_4$. For certifying, the Kubelka-Munk equation was applied to estimate the bandgap energy (E_g) of semiconductors (Qiu et al., 2019):

$$(\alpha h\upsilon)^2 = A\left(h\upsilon - E_g\right)^{n/2} \quad (2)$$

where α, h, υ, and A are the diffuse absorption coefficient, Planck's constant, light frequency, and constant, respectively. As depicted in Figures 9B–D, direct bandgap energies were calculated from the tangent line obtained by plotting $(\alpha h\upsilon)^2$ vs energy (hυ). For UiO-66, $CoFe_2O_4$, and $CoFe_2O_4$@UiO-66 composite, the estimated E_g values are approximately 3.84, 1.63, and 2.74 eV, respectively. In the case of the composite, the relatively reduced bandgap observed might be assigned to the interface formed between UiO-66 and the narrow bandgap $CoFe_2O_4$ particles, resulting in more effective absorption of the solar spectrum and eventually better photocatalytic response.

3.3 Photoelectrochemical properties

Photoluminescence (PL) spectra were obtained to evaluate charge separation and transmission efficiency over different catalysts. In theory, the lower the PL intensity, the lower the reintegration of the charge carriers, which is advantageous to the

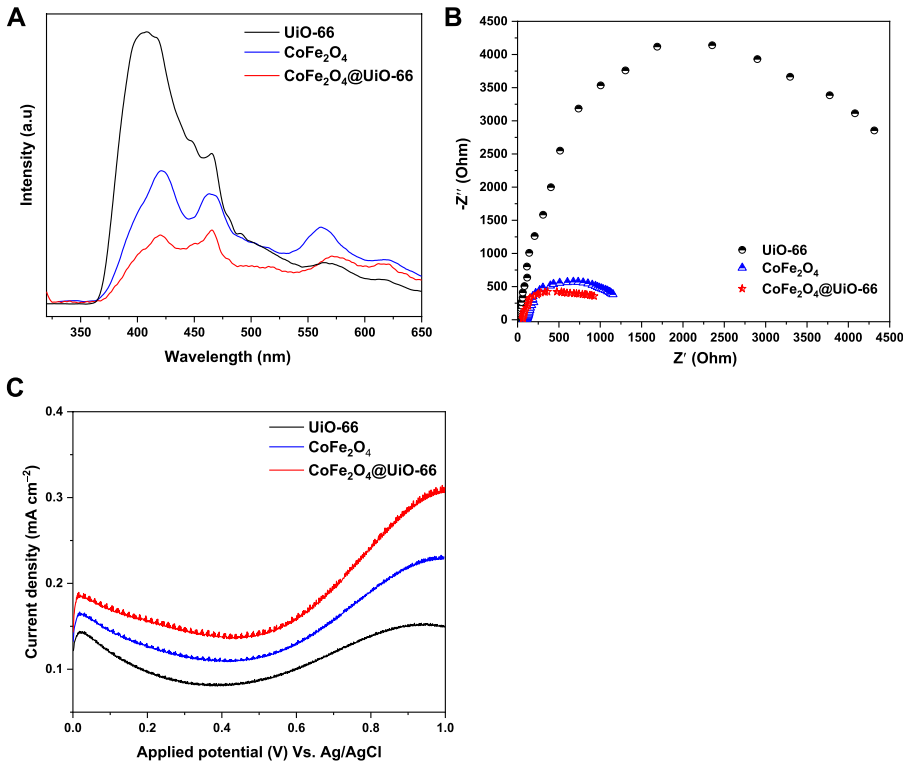

FIGURE 10
PL emission spectra **(A)**, EIS Nyquist **(B)**, and LSV curves **(C)** of UiO-66, $CoFe_2O_4$ and $CoFe_2O_4$@UiO-66 composite.

photocatalytic reaction (He et al., 2021). As revealed in Figure 10A, the PL spectral intensity decreased in the order of UiO-66 > $CoFe_2O_4$ > $CoFe_2O_4$@UiO-66, where, pristine UiO-66 exhibited the highest peak intensity at around 407 nm. Conversely, upon coupling with $CoFe_2O_4$ particles, the PL intensity is markedly suppressed and the signal is displaced to a higher wavelength (466 nm). Thus, it can be deduced that the formation of core-shell heterostructure significantly quenched the recombination of photoinduced charge carriers, accelerating the migration rate.

The photoelectrochemical characterizations were further investigated by electrochemical impedance spectroscopy (EIS) and linear sweep voltammetry (LSV) to verify the charge transfer and current density, thereby determining the photocatalytic performance of catalysts. Consistent with the findings of the PL analysis, EIS Nyquist plots displayed the same tendency (Figure 10B). Basically, the smaller the semicircle diameter in EIS plots, the lower the charge transfer resistance (Zhang et al., 2022). In this study, it is interestingly noted that $CoFe_2O_4$@UiO-66 displayed a smaller Nyquist arc radius than those of parent UiO-66 and $CoFe_2O_4$, reaffirming the depletion in charge transfer resistance and enhancement of charge carriers separation by constructing heterojunction. In addition, LSV profiles of as-synthesized catalysts are represented in Figure 10C. As can be seen, UiO-66 displayed the lowest current density (0.15 mA cm^{-2}), owing to inefficient utilization of visible light. In contrast, the current density is significantly improved to 0.31 mA cm^{-2} over $CoFe_2O_4$@UiO-66. On the other side, the anodic currents in LSV curves demonstrated the n-type semiconductor nature of the as-synthesized catalysts (Quach et al., 2022). To summarize, these findings assert that the successful interfacial contact between UiO-66 and $CoFe_2O_4$ can sufficiently hinder the charge recombination dilemma and induce effective separation of photoinduced carriers, leading to swift surface reaction dynamics and better photocatalytic activity.

3.4 Photocatalytic performance

The photocatalytic activities of bare and composite catalysts were studied through the degradation of MB and MO dyes as representative pollutants under simulated solar irradiation. Obviously, under dark conditions, the dye adsorption capacity follows the order UiO-66 > $CoFe_2O_4$@UiO-66 > $CoFe_2O_4$ (Figures 11A, B). In comparison with pure $CoFe_2O_4$, the adsorption capacity of $CoFe_2O_4$@UiO-66 composite is significantly boosted owing to the abundant exposed

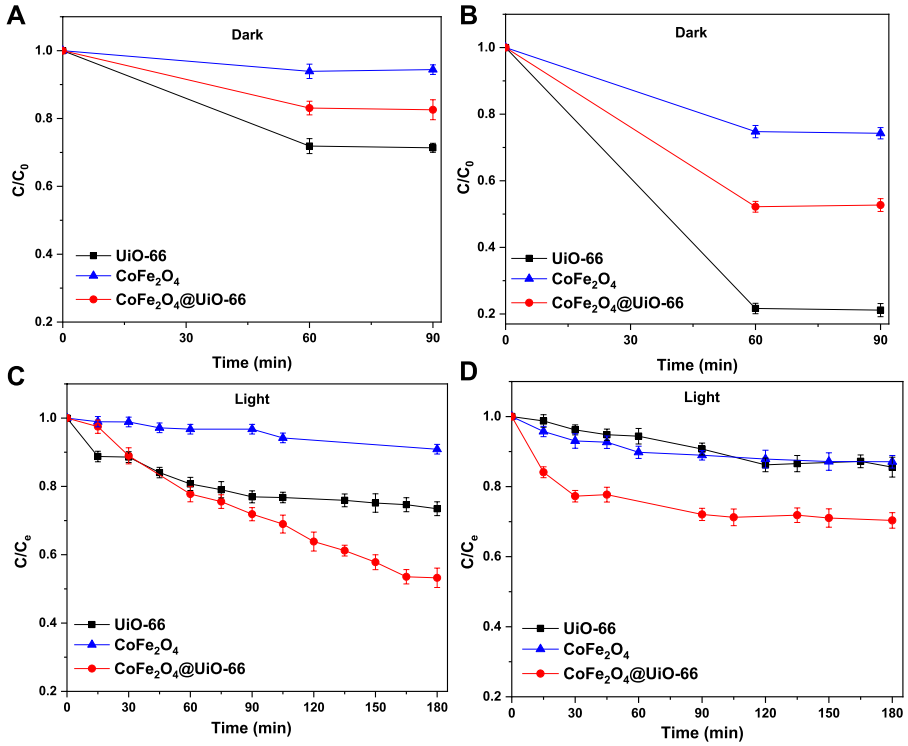

FIGURE 11
Adsorption and photodegradation performance of as-synthesized photocatalysts for removal of MB **(A,C)** and MO **(B,D)** dyes.

adsorption sites and internal porous structure of the outer UiO-66 shell. Noteworthy, the removal efficiencies of the different photocatalysts for MO dye are about 3.0–4.4-folds higher than that for MB dye. In general, the surface charge of the particles can prominently influence their interaction with target pollutants, affecting the adsorption capacity (Sohrabnezhad and Moghadamy, 2022). In this regard, the Zeta potentials of the as-synthesized catalysts were measured and the findings are depicted in (Supplementary Figure S3). As observed, all samples possess positive charges with a potential of +17.2, + 19.5, and +23.8 mV for UiO-66, $CoFe_2O_4$, and $CoFe_2O_4$@UiO-66, respectively. Hence, anionic dye molecules are effectively adsorbed to the surface by electrostatic interaction, which is proposed as the predominated removal mechanism during the adsorption process. Following the accomplishment of adsorption-desorption equilibrium, the equilibrium dye concentration (C_e) was applied as the initial concentration. As presented in Figures 11C, D, upon simulated solar illumination, pristine UiO-66 and $CoFe_2O_4$ exhibited low degradation efficiency due to the weak visible light harvesting and ineffective segregation of photogenerated carriers, respectively. By comparison, considerable photocatalytic degradation was attained in presence of $CoFe_2O_4$@UiO-66 composite, with a 20%–40% increase in degradation efficiency (Figure 12A). The UV-Vis spectral changes of MB and MO dyes over $CoFe_2O_4$@UiO-66 photocatalyst at different illumination times are revealed in Figures 12B, C.

To further elucidate the photodegradation process, kinetic curves were plotted and rate constants k) were calculated. (Supplementary Figure S4) illustrates the pseudo-first-order kinetic equation to define the reaction rate constant of different samples following Eq. 3 (Yi et al., 2019):

$$(\ln (C_e/C) = kt \quad (3)$$

where k is the first-order rate coefficient (min^{-1}), C_e is the dye concentration at equilibrium and C is the concentration at time t. It is noteworthy that among the three catalysts, the $CoFe_2O_4$@UiO-66 composite possessed a greater rate constant, which is consistent with the photocatalytic results. As evident, the heterojunction constructed between UiO-66 and $CoFe_2O_4$ simultaneously reduced the charge carrier recombination and increased the photon absorption capacity, resulting in a faster photocatalytic reaction. The photocatalytic activity of $CoFe_2O_4$@UiO-66 composite for dye degradation was further compared with the previously reported photocatalysts (Table 2). Overall, the $CoFe_2O_4$@UiO-66 composite displayed outstanding efficiency for the degradation of dyes at high initial concentrations.

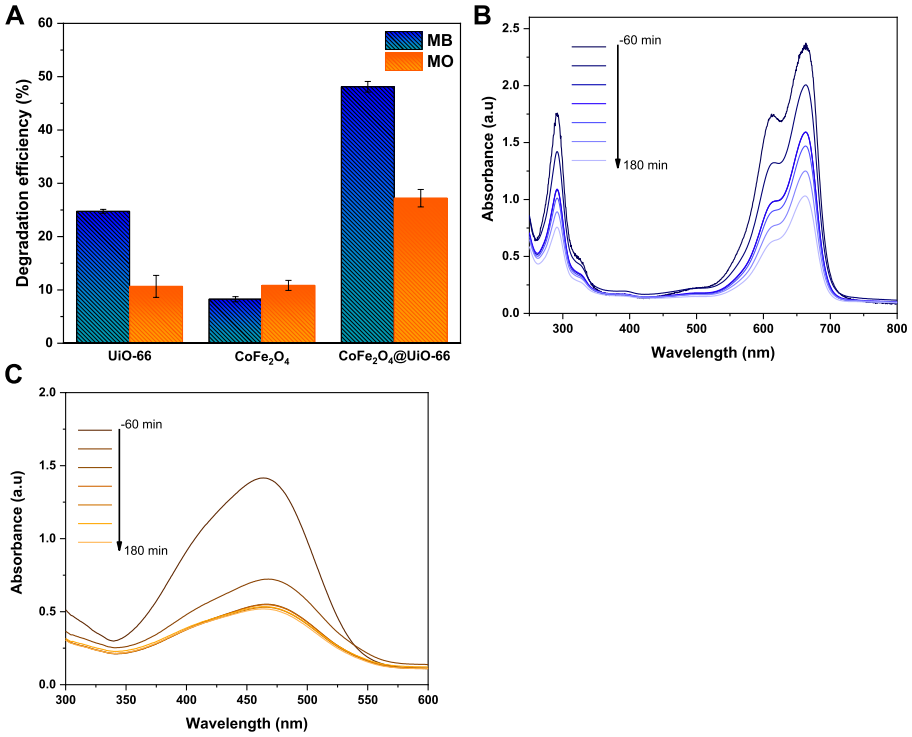

FIGURE 12
The photodegradation efficiency of as-synthesized photocatalysts **(A)**, UV-Vis absorption spectra for degradation of MB **(B)** and MO **(C)** dyes over $CoFe_2O_4$@UiO-66.

3.5 Proposed photocatalytic mechanism

To explore the possible mechanism for the photocatalytic degradation of MB and MO dyes, radical trapping experiments were performed over $CoFe_2O_4$@UiO-66 composite under simulated solar irradiation. EDTA-2Na, BQ, and IPA were utilized separately in the degradation system as h^+, $\bullet O_2^-$, and •OH scavengers, respectively. As observed in Figure 13, all the reactive substances are contributed to the catalytic process. Nevertheless, EDTA-2Na has the most significant impact on the degradation reaction. When EDTA-2Na is added, the degradation rate decreased drastically to 12% and 15% for MB and MO, respectively. In the meanwhile, upon the introduction of BQ and IPA, a moderate influence on the degradation efficiency can be seen. This implies that photogenerated holes are the dominant active species, while $\bullet O_2^-$ and •OH possess a certain contribution to the photocatalytic reaction.

For more insights into the mechanism of photogenerated charge separation, Mott-Schottky (M–S) measurement was further implemented to investigate the electronic band structure and the semiconductivity nature of UiO-66 and $CoFe_2O_4$. The positive slope of the tangent lines depicted in Figures 14A, B suggests that both materials are typical n-type semiconductors (Shen et al., 2015a), which is in agreement with the LSV results. The results showed that the flat band potential (E_{FB}) of UiO-66 and $CoFe_2O_4$ are set as –0.23 and –0.31 V vs. Ag/AgCl, respectively. Subsequently, the E_{FB} (vs. NHE) could be determined as follows (Man et al., 2022):

$$E_{(NHE,\,pH=7)} = E_{Ag/AgCl} - 0.059\,(7 - \text{pH of the electrolyte}) + 0.198 \quad (4)$$

Thence, the E_{FB} of UiO-66 and $CoFe_2O_4$ is –0.24 and –0.36 V (vs NHE), respectively. In general, the conduction band (E_{CB}) potential for n-type semiconductors is approximately 0.1–0.2 V more negative than the flat band potential (Ishikawa et al., 2002). Accordingly, the corresponding (E_{CB}) potential of UiO-66 and $CoFe_2O_4$ can be calculated as –0.44 and –0.56 V (vs. NHE), respectively. From the bandgap values obtained above, the valence band (E_{VB}) potential can be calculated using Eq. 4:

$$E_{VB} = E_g + E_{CB} \quad (5)$$

Subsequently, the E_{VB} potential of UiO-66 and $CoFe_2O_4$ is determined as 3.40 and 1.07 V (vs. NHE), respectively.

In the light of the aforementioned findings and discussion, the plausible reaction mechanism for photocatalytic degradation of MB and MO over $CoFe_2O_4$@UiO-66 photocatalyst is proposed (Figure 15). Upon simulated sunlight irradiation, both UiO-66

TABLE 2 Comparison of photocatalytic performance of $CoFe_2O_4$@UiO-66 with other reported photocatalysts for degradation of MB and MO.

Photocatalyst	Dye concentration (mg/L)	Catalyst amount (mg/L)	Light source	Irradiation time (min)	Removal rate (%)	Ref
MB dye						
Fe-UiO-66	20	10	60 W white LED lamp	160	84	Hosseini et al. (2022)
g-C_3N_4–xClx/0.5 M HCl	3	25	1000 W Xe lamp (λ ≥ 420 nm)	180	97	Bai et al. (2020)
$Co_{0.1}Mg_{0.9}Fe_2O_4$	10	10	A halogen lamp (intensity: 70 mWcm^2)	240	80	Dojcinovic et al. (2021)
α-Fe_2O_3@UiO-66	13	100	300 W Xe lamp (λ ≥ 420 nm)	50	100	Zhang et al. (2019a)
UiO-66/g-C_3N_4 UC10:10	10	50	350 W Xe lamp (λ > 420 nm)	240	99	Zhang et al. (2018)
30% $CuNb_2O_6$/g-C_3N_4	10	20	500 W Xe lamp	150	98.5	Ahmad et al. (2022)
S–N-co-doped-$CoFe_2O_4$@rGO@TiO_2	5	8	300 W Xe lamp (λ > 420 nm)	360	94	Wei et al. (2019)
$CoFe_2O_4$@UiO-66	100	50	150 W Xe lamp	180	56.7	This work
MO dye						
UiO-66-NH_2@CNT (3 wt%)	15	30	100 W LED lamp	30	93	Abdi et al. (2021)
OV-BOC	10	100	300 W Xe lamp (λ > 400 nm)	120	82	Zhao et al. (2019)
40 wt%-AgBr/CeO_2	30	50	300 W Xe lamp (λ ≥ 400 nm)	180	93	Chen et al. (2021)
UiO-66/$BiFeO_3$	10	50	250 W high-pressure Hg lamp (λ > 400 nm)	180	88.7	Bargozideh et al. (2020)
Au-$CoFe_2O_4$/MoS_2	50	70	300 W iodine tungsten lamp	120	99	Jia et al. (2019)
rGO@In_2S_3@UiO-66	15	30	500 W Xe lamp (λ = 420 nm)	60	98.1	Gan et al. (2019)
3% TiO_2/g-C_3N_4	10	1,000	500 W Xe lamp (simulated sunlight)	80	62.6	Huang et al. (2016)
$CoFe_2O_4$@UiO-66	100	50	150 W Xe lamp	180	63.3	This work

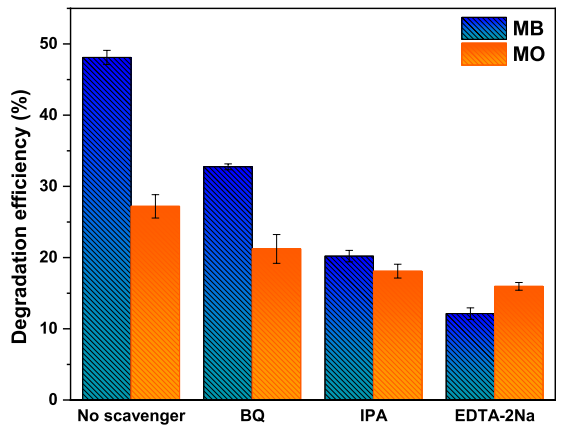

FIGURE 13
The effect of different quenchers on the photocatalytic activity of $CoFe_2O_4$@UiO-66 for degradation of MB and MO dyes.

and $CoFe_2O_4$ are excited, generating electrons (e^-) and holes (h^+) in their CB and VB, respectively. Since, the CB potential of $CoFe_2O_4$ (−0.56 V) is more negative than the LUMO of UiO-66 (−0.44 V), the excited electrons can directly transfer through the interface channels formed by the heterojunction to the LUMO of UiO-66, suppressing the recombination of photogenerated carriers (Wang et al., 2021d; Gao et al., 2021). Subsequently, the photoinduced electrons at LUMO of UiO-66 can reduce the dissolved oxygen to yield $\bullet O_2^-$ radicals. Meanwhile, the photogenerated holes would transfer from the VB of UiO-66 (+3.40 V) to the VB of $CoFe_2O_4$ (+1.07 V). However, as the VB potential of $CoFe_2O_4$ (+1.07 V) is lower than the redox potential of $^-OH/\bullet OH$ (1.99 V vs NHE), the photogenerated holes cannot oxidize H_2O to produce •OH radicals (Wang et al., 2022). Instead, the accumulated holes promptly degrade the dye molecules because of their strong oxidation properties. Otherwise, •OH reactive radicals could be indirectly generated through $\bullet O_2^-$ radicals at the CB of the photocatalyst (Zou et al., 2021). This is consistent with the results of quenching

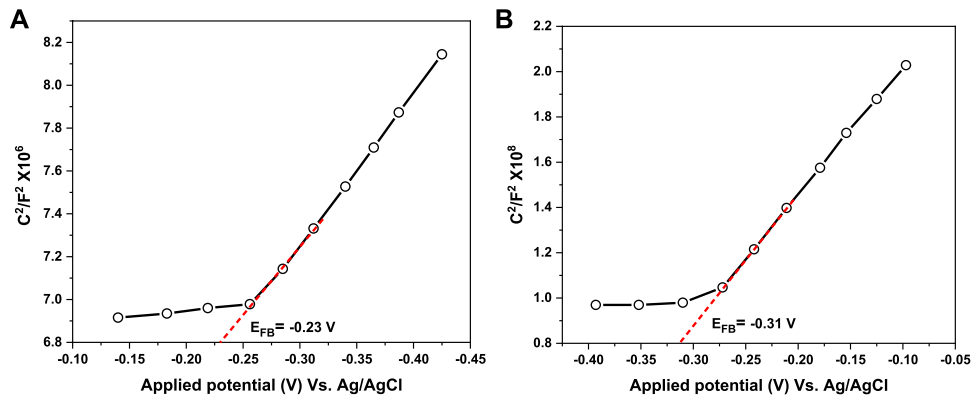

FIGURE 14
Mott-Schottky plots of UiO-66 **(A)** and $CoFe_2O_4$ **(B)**.

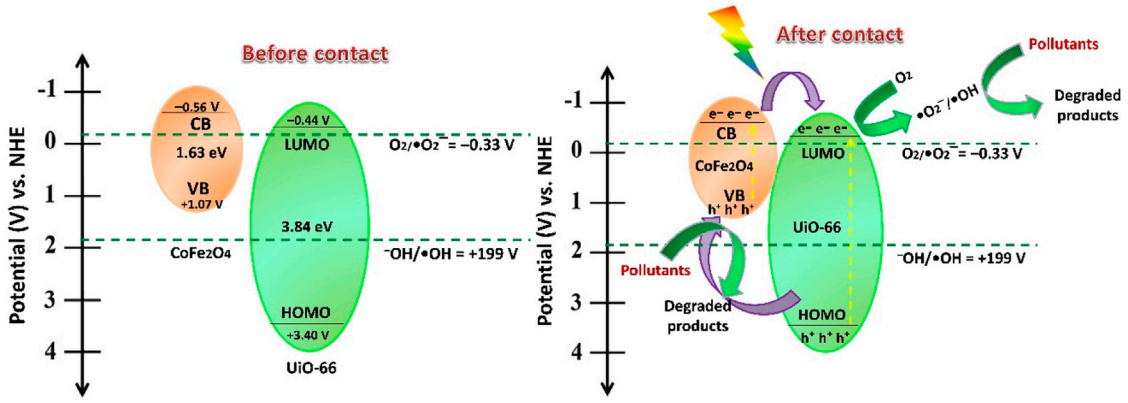

FIGURE 15
A proposed photocatalytic mechanism for dye degradation over $CoFe_2O_4$@UiO-66 heterojunction under simulative solar irradiation.

experiments, indicating the construction of a staggered type II heterojunction energy band alignment near the interface of UiO-66 and $CoFe_2O_4$. The following equations may summarize the degradation process:

$$CoFe_2O_4@UiO-66 + h\upsilon \rightarrow e^- + h^+ \quad (6)$$

$$e^- + O_2 \rightarrow \bullet O_2^- \quad (7)$$

$$\bullet O_2^- + 2h^+ + 2e^- \rightarrow H_2O_2 \quad (8)$$

$$H_2O_2 + 2e^- \rightarrow {}^-OH + \bullet OH \quad (9)$$

$$\text{Organic dye} + h^+ + \bullet OH + \bullet O_2^- \rightarrow \text{degradation products} \quad (10)$$

4 Conclusion

In summary, a novel $CoFe_2O_4$@UiO-66 core-shell heterojunction photocatalyst was successfully synthesized through a simple solvothermal route. In comparison with the UV-driven UiO-66 catalyst, the $CoFe_2O_4$@UiO-66 heterojunction displayed an enhanced photo-responsive capacity in the visible region with an absorption band of ~467 nm. This can be certified by the reduction of bandgap energy from 3.84 eV for UiO-66 to 2.74 eV for the composite material. The $CoFe_2O_4$@UiO-66 composite exhibited better performance than either UiO-66 or $CoFe_2O_4$ towards photodegradation of organic dyes at a high initial concentration under simulated solar light irradiation. The overall removal efficiency of dyes (100 mg/L) over $CoFe_2O_4$@UiO-66 (50 mg/L) reached >60% within 180 min irradiation. Moreover, the photoluminescence, impedance, and current density studies showed an effective charge separation and transfer over the $CoFe_2O_4$@UiO-66 composite. This was mainly ascribed to the tight interfacial contact formed through the heterojunction, which suppressed the charge recombination rate, thereby improving the photocatalytic activity. From radical scavenging

experiments and Mott-Schottky analysis, it can be inferred that h^+ had the primarily significant contribution during the photocatalytic process. This study paved the way to design MOF-based core-shell heterostructured photocatalysts with more active sites, good optical properties, and enhanced photocatalytic activity for various environmental applications.

Data availability statement

The original contributions presented in the study are included in the article/Supplementary Material, further inquiries can be directed to the corresponding author.

Author contributions

YA: Writing -original draft, Conceptualization, Investigation, Methodology and Analysis. MS: Investigation. RA: Investigation. AZ: Supervision, Conceptualization, Investigation, review and editing.

Acknowledgments

The authors gratefully acknowledge the National Institute of Oceanography and Fisheries (NIOF) for complementary financial support and Aaisha M. Naim, MSc student at the Faculty of Postgraduate Studies for Advanced Sciences for her assistance.

Conflict of interest

The authors declare that the research was conducted in the absence of any commercial or financial relationships that could be construed as a potential conflict of interest.

Publisher's note

All claims expressed in this article are solely those of the authors and do not necessarily represent those of their affiliated organizations, or those of the publisher, the editors and the reviewers. Any product that may be evaluated in this article, or claim that may be made by its manufacturer, is not guaranteed or endorsed by the publisher.

Supplementary material

The Supplementary Material for this article can be found online at: https://www.frontiersin.org/articles/10.3389/fchem.2022.1102920/full#supplementary-material

References

Abdi, J., Banisharif, F., and Khataee, A. (2021). Amine-functionalized Zr-MOF/CNTs nanocomposite as an efficient and reusable photocatalyst for removing organic contaminants. *J. Mol. Liq.* 334, 116129. doi:10.1016/j.molliq.2021.116129

Ahmad, N., Kuo, C. F. J., and Mustaqeem, M. (2022). Synthesis of novel CuNb2O6/g-C3N4 binary photocatalyst towards efficient visible light reduction of Cr (VI) and dyes degradation for environmental remediation. *Chemosphere* 298, 134153. doi:10.1016/j.chemosphere.2022.134153

Al-Mamun, M., Kader, S., Islam, M., and Khan, M. (2019). Photocatalytic activity improvement and application of UV-TiO2 photocatalysis in textile wastewater treatment: A review. *J. Environ. Chem. Eng.* 7, 103248. doi:10.1016/j.jece.2019.103248

Ba-Abbad, M. M., Kadhum, A. A. H., Mohamad, A. B., Takriff, M. S., and Sopian, K. (2013). Visible light photocatalytic activity of Fe3+-doped ZnO nanoparticle prepared via sol–gel technique. *Chemosphere* 91, 1604–1611. doi:10.1016/j.chemosphere.2012.12.055

Bai, X., Wang, X., Lu, X., Liang, Y., Li, J., Wu, L., et al. (2020). Surface defective g-C3N4–Cl with unique spongy structure by polarization effect for enhanced photocatalytic removal of organic pollutants. *J. Hazard. Mater.* 398, 122897. doi:10.1016/j.jhazmat.2020.122897

Bargozideh, S., Tasviri, M., Shekarabi, S., and Daneshgar, H. (2020). Magnetic BiFeO 3 decorated UiO-66 as ap–n heterojunction photocatalyst for simultaneous degradation of a binary mixture of anionic and cationic dyes. *New J. Chem.* 44, 13083–13092. doi:10.1039/d0nj02594a

Bariki, R., Majhi, D., Das, K., Behera, A., and Mishra, B. (2020). Facile synthesis and photocatalytic efficacy of UiO-66/CdIn2S4 nanocomposites with flowerlike 3D-microspheres towards aqueous phase decontamination of triclosan and H2 evolution. *Appl. Catal. B Environ.* 270, 118882. doi:10.1016/j.apcatb.2020.118882

Basak, M., Rahman, M. L., Ahmed, M. F., Biswas, B., and Sharmin, N. (2021). Calcination effect on structural, morphological and magnetic properties of nano-sized CoFe2O4 developed by a simple co-precipitation technique. *Mater. Chem. Phys.* 264, 124442. doi:10.1016/j.matchemphys.2021.124442

Bi, F., Zhang, X., Chen, J., Yang, Y., and Wang, Y. (2020). Excellent catalytic activity and water resistance of UiO-66-supported highly dispersed Pd nanoparticles for toluene catalytic oxidation. *Appl. Catal. B Environ.* 269, 118767. doi:10.1016/j.apcatb.2020.118767

Cao, J., Yang, Z.-h., Xiong, W.-p., Zhou, Y.-y., Peng, Y.-r., Li, X., et al. (2018). One-step synthesis of Co-doped UiO-66 nanoparticle with enhanced removal efficiency of tetracycline: Simultaneous adsorption and photocatalysis. *Chem. Eng. J.* 353, 126–137. doi:10.1016/j.cej.2018.07.060

Chakhtouna, H., Benzeid, H., Zari, N., and Bouhfid, R. (2021). Functional CoFe2O4-modified biochar derived from banana pseudostem as an efficient adsorbent for the removal of amoxicillin from water. *Sep. Purif. Technol.* 266, 118592. doi:10.1016/j.seppur.2021.118592

Chen, C., Chen, D., Xie, S., Quan, H., Luo, X., and Guo, L. (2017). Adsorption behaviors of organic micropollutants on zirconium metal–organic framework UiO-66: Analysis of surface interactions. *ACS Appl. Mater. interfaces* 9, 41043–41054. doi:10.1021/acsami.7b13443

Chen, C., Wang, D., Li, Y., Huang, H., and Ke, Y. (2021). Flower-like AgBr/CeO2 Z-scheme heterojunction photocatalyst with enhanced visible light photocatalytic and antibacterial activities. *Appl. Surf. Sci.* 565, 150534. doi:10.1016/j.apsusc.2021.150534

Chen, T., Du, P., Jiang, W., Liu, J., Hao, G., Gao, H., et al. (2016). A facile one-pot solvothermal synthesis of CoFe 2 O 4/RGO and its excellent catalytic activity on thermal decomposition of ammonium perchlorate. *RSC Adv.* 6, 83838–83847. doi:10.1039/c6ra16448j

Cheng, C., Fang, J., Lu, S., Cen, C., Chen, Y., Ren, L., et al. (2016). Zirconium metal-organic framework supported highly-dispersed nanosized BiVO4 for enhanced visible-light photocatalytic applications. *J. Chem. Technol. Biotechnol.* 91, 2785–2792. doi:10.1002/jctb.4885

Connolly, B. M., Madden, D. G., Wheatley, A. E., and Fairen-Jimenez, D. (2020). Shaping the future of fuel: Monolithic metal–organic frameworks for high-density gas storage. *J. Am. Chem. Soc.* 142, 8541–8549. doi:10.1021/jacs.0c00270

Deng, J., Shao, Y., Gao, N., Tan, C., Zhou, S., and Hu, X. (2013). CoFe2O4 magnetic nanoparticles as a highly active heterogeneous catalyst of oxone for the degradation of diclofenac in water. *J. Hazard. Mater.* 262, 836–844. doi:10.1016/j.jhazmat.2013.09.049

Dey, A., and Gogate, P. R. (2021). Nanocomposite photocatalysts-based wastewater treatment. *Handb. Nanomater. Wastewater Treat.* 2021, 779–809. doi:10.1016/B978-0-12-821496-1.00022-2

Dihom, H. R., Al-Shaibani, M. M., Mohamed, R. M. S. R., Al-Gheethi, A. A., Sharma, A., and Khamidun, M. H. B. (2022). Photocatalytic degradation of disperse azo dyes in textile wastewater using green zinc oxide nanoparticles synthesized in plant extract: A critical review. *J. Water Process Eng.* 47, 102705. doi:10.1016/j.jwpe.2022.102705

Ding, J., Yang, Z., He, C., Tong, X., Li, Y., Niu, X., et al. (2017). UiO-66 (Zr) coupled with Bi2MoO6 as photocatalyst for visible-light promoted dye degradation. *J. colloid interface Sci.* 497, 126–133. doi:10.1016/j.jcis.2017.02.060

Dojcinovic, M. P., Vasiljevic, Z. Z., Pavlovic, V. P., Barisic, D., Pajic, D., Tadic, N. B., et al. (2021). Mixed Mg–Co spinel ferrites: Structure, morphology, magnetic and photocatalytic properties. *J. Alloys Compd.* 855, 157429. doi:10.1016/j.jallcom.2020.157429

Ebrahim, A. M., and Bandosz, T. J. (2013). Ce (III) doped Zr-based MOFs as excellent NO2 adsorbents at ambient conditions. *ACS Appl. Mater. Interfaces* 5, 10565–10573. doi:10.1021/am402305u

Esmat, M., Farghali, A. A., Khedr, M. H., and El-Sherbiny, I. M. (2017). Alginate-based nanocomposites for efficient removal of heavy metal ions. *Int. J. Biol. Macromol.* 102, 272–283. doi:10.1016/j.ijbiomac.2017.04.021

Feng, C., Lu, Z., Zhang, Y., Liang, Q., Zhou, M., Li, X., et al. (2022). A magnetically recyclable dual Z-scheme GCNQDs-CoTiO3/CoFe2O4 composite photocatalyst for efficient photocatalytic degradation of Oxytetracycline. *Chem. Eng. J.* 435, 134833. doi:10.1016/j.cej.2022.134833

Franking, R., Li, L., Lukowski, M. A., Meng, F., Tan, Y., Hamers, R. J., et al. (2013). Facile post-growth doping of nanostructured hematite photoanodes for enhanced photoelectrochemical water oxidation. *Energy & Environ. Sci.* 6, 500–512. doi:10.1039/c2ee23837c

Gan, C., Xu, C., Wang, H., Zhang, N., Zhang, J., and Fang, Y. (2019). Facile synthesis of rGO@ In2S3@ UiO-66 ternary composite with enhanced visible-light photodegradation activity for methyl orange. *J. Photochem. Photobiol. A Chem.* 384, 112025. doi:10.1016/j.jphotochem.2019.112025

Gao, C., Wang, J., Xu, H., and Xiong, Y. (2017). Coordination chemistry in the design of heterogeneous photocatalysts. *Chem. Soc. Rev.* 46, 2799–2823. doi:10.1039/c6cs00727a

Gao, D., Zhang, Y., Yan, H., Li, B., He, Y., Song, P., et al. (2021). Construction of UiO-66@ MoS2 flower-like hybrids through electrostatically induced self-assembly with enhanced photodegradation activity towards lomefloxacin. *Sep. Purif. Technol.* 265, 118486. doi:10.1016/j.seppur.2021.118486

Görmez, Ö., Yakar, E., Gözmen, B., Kayan, B., and Khataee, A. (2022). CoFe2O4 nanoparticles decorated onto graphene oxide and graphitic carbon nitride layers as a separable catalyst for ultrasound-assisted photocatalytic degradation of Bisphenol-A. *Chemosphere* 288, 132663. doi:10.1016/j.chemosphere.2021.132663

Han, W., Shao, L.-H., Sun, X.-J., Liu, Y.-H., Zhang, F.-M., Wang, Y., et al. (2022). Constructing Cu ion sites in MOF/COF heterostructure for noble-metal-free photoredox catalysis. *Appl. Catal. B Environ.* 317, 121710. doi:10.1016/j.apcatb.2022.121710

Han, Y., Liu, M., Li, K., Sun, Q., Zhang, W., Song, C., et al. (2017). *In situ* synthesis of titanium doped hybrid metal–organic framework UiO-66 with enhanced adsorption capacity for organic dyes. *Inorg. Chem. Front.* 4, 1870–1880. doi:10.1039/c7qi00437k

He, Y., Wang, D., Li, X., Fu, Q., Yin, L., Yang, Q., et al. (2021). Photocatalytic degradation of tetracycline by metal-organic frameworks modified with Bi2WO6 nanosheet under direct sunlight. *Chemosphere* 284, 131386. doi:10.1016/j.chemosphere.2021.131386

Holkar, C. R., Jadhav, A. J., Pinjari, D. V., Mahamuni, N. M., and Pandit, A. B. (2016). A critical review on textile wastewater treatments: Possible approaches. *J. Environ. Manag.* 182, 351–366. doi:10.1016/j.jenvman.2016.07.090

Hosseini, M.-S., Abbasi, A., and Masteri-Farahani, M. (2022). Improving the photocatalytic activity of NH2-UiO-66 by facile modification with Fe (acac) 3 complex for photocatalytic water remediation under visible light illumination. *J. Hazard. Mater.* 425, 127975. doi:10.1016/j.jhazmat.2021.127975

Huang, S., Zhong, J., Li, J., Chen, J., Xiang, Z., Hu, W., et al. (2016). Z-scheme TiO2/g-C3N4 composites with improved solar-driven photocatalytic performance deriving from remarkably efficient separation of photo-generated charge pairs. *Mater. Res. Bull.* 84, 65–70. doi:10.1016/j.materresbull.2016.07.036

Ishikawa, A., Takata, T., Kondo, J. N., Hara, M., Kobayashi, H., and Domen, K. (2002). Oxysulfide Sm2Ti2S2O5 as a stable photocatalyst for water oxidation and reduction under visible light irradiation (λ≤ 650 nm). *J. Am. Chem. Soc.* 124, 13547–13553. doi:10.1021/ja0269643

Ivanchikova, I. D., Lee, J. S., Maksimchuk, N. V., Shmakov, A. N., Chesalov, Y. A., Ayupov, A. B., et al. (2014). Highly selective H2O2-based oxidation of alkylphenols to p-benzoquinones over MIL-125 metal–organic frameworks. *Eur. J. Inorg. Chem.* 2014, 132–139. doi:10.1002/ejic.201301098

Jabbar, Z. H., and Graimed, B. H. (2022). Recent developments in industrial organic degradation via semiconductor heterojunctions and the parameters affecting the photocatalytic process: A review study. *J. Water Process Eng.* 47, 102671. doi:10.1016/j.jwpe.2022.102671

Jia, Y., Ma, H., and Liu, C. (2019). Au nanoparticles enhanced Z-scheme Au-CoFe2O4/MoS2 visible light photocatalyst with magnetic retrievability. *Appl. Surf. Sci.* 463, 854–862. doi:10.1016/j.apsusc.2018.09.008

Jing, L., Xu, Y., Huang, S., Xie, M., He, M., Xu, H., et al. (2016). Novel magnetic CoFe2O4/Ag/Ag3VO4 composites: Highly efficient visible light photocatalytic and antibacterial activity. *Appl. Catal. B Environ.* 199, 11–22. doi:10.1016/j.apcatb.2016.05.049

Johnson, M., Gaffney, C., White, V., Bechelli, J., Balaraman, R., and Trad, T. (2020). Non-hydrolytic synthesis of caprylate capped cobalt ferrite nanoparticles and their application against Erwinia carotovora and Stenotrophomonas maltophilia. *J. Mater. Chem. B* 8, 10845–10853. doi:10.1039/d0tb02283g

Kefeni, K. K., and Mamba, B. B. (2020). Photocatalytic application of spinel ferrite nanoparticles and nanocomposites in wastewater treatment: Review. *Sustain. Mater. Technol.* 23, e00140. doi:10.1016/j.susmat.2019.e00140

Khosroshahi, N., Karimi, M., Taghvaei, T., and Safarifard, V. (2021). Ultrasound-assisted synthesis of CoFe2O4/Ce-UiO-66 nanocomposite for photocatalytic aerobic oxidation of aliphatic alcohols. *Mater. Today Chem.* 22, 100582. doi:10.1016/j.mtchem.2021.100582

Kreft, S., Wei, D., Junge, H., and Beller, M. (2020). Recent advances on TiO2-based photocatalytic CO2 reduction. *EnergyChem* 2, 100044. doi:10.1016/j.enchem.2020.100044

Lee, I., Choi, S., Lee, H. J., and Oh, M. (2015). Hollow metal–organic framework microparticles assembled via a self-templated formation mechanism. *Cryst. Growth & Des.* 15, 5169–5173. doi:10.1021/acs.cgd.5b00919

Lei, Z., Xue, Y., Chen, W., Qiu, W., Zhang, Y., Horike, S., et al. (2018). MOFs-based heterogeneous catalysts: New opportunities for energy-related CO2 conversion. *Adv. Energy Mater.* 8, 1801587. doi:10.1002/aenm.201801587

Li, D., Kassymova, M., Cai, X., Zang, S.-Q., and Jiang, H.-L. (2020). Photocatalytic CO2 reduction over metal-organic framework-based materials. *Coord. Chem. Rev.* 412, 213262. doi:10.1016/j.ccr.2020.213262

Liang, H., Guo, J., Yu, M., Zhou, Y., Zhan, R., Liu, C., et al. (2021). Porous loofah-sponge-like ternary heterojunction g-C3N4/Bi2WO6/MoS2 for highly efficient photocatalytic degradation of sulfamethoxazole under visible-light irradiation. *Chemosphere* 279, 130552. doi:10.1016/j.chemosphere.2021.130552

Liang, Z., Zhao, R., Qiu, T., Zou, R., and Xu, Q. (2019). Metal-organic framework-derived materials for electrochemical energy applications. *EnergyChem* 1, 100001. doi:10.1016/j.enchem.2019.100001

Liu, B., Liu, X., Liu, J., Feng, C., Li, Z., Li, C., et al. (2018). Efficient charge separation between UiO-66 and ZnIn2S4 flowerlike 3D microspheres for photoelectronchemical properties. *Appl. Catal. B Environ.* 226, 234–241. doi:10.1016/j.apcatb.2017.12.052

Liu, M., Xing, Z., Li, Z., and Zhou, W. (2021). Recent advances in core–shell metal organic frame-based photocatalysts for solar energy conversion. *Coord. Chem. Rev.* 446, 214123. doi:10.1016/j.ccr.2021.214123

Ma, S., Zhan, S., Jia, Y., and Zhou, Q. (2015). Highly efficient antibacterial and Pb (II) removal effects of Ag-CoFe2O4-GO nanocomposite. *ACS Appl. Mater. interfaces* 7, 10576–10586. doi:10.1021/acsami.5b02209

Man, Z., Meng, Y., Lin, X., Dai, X., Wang, L., and Liu, D. (2022). Assembling UiO-66@ TiO2 nanocomposites for efficient photocatalytic degradation of dimethyl sulfide. *Chem. Eng. J.* 431, 133952. doi:10.1016/j.cej.2021.133952

Mathew, D. S., and Juang, R.-S. (2007). An overview of the structure and magnetism of spinel ferrite nanoparticles and their synthesis in microemulsions. *Chem. Eng. J.* 129, 51–65. doi:10.1016/j.cej.2006.11.001

Mirhosseini-Eshkevari, B., Esnaashari, M., and Ghasemzadeh, M. A. (2019). Novel Brönsted acidic ionic liquids confined in UiO-66 nanocages for the synthesis of dihydropyrido [2, 3-d] pyrimidine derivatives under solvent-free conditions. *ACS omega* 4, 10548–10557. doi:10.1021/acsomega.9b00178

Mmelesi, O. K., Masunga, N., Kuvarega, A., Nkambule, T. T., Mamba, B. B., and Kefeni, K. K. (2021). Cobalt ferrite nanoparticles and nanocomposites: Photocatalytic, antimicrobial activity and toxicity in water treatment. *Mater. Sci. Semicond. Process.* 123, 105523. doi:10.1016/j.mssp.2020.105523

Molavi, H., Hakimian, A., Shojaei, A., and Raeiszadeh, M. (2018). Selective dye adsorption by highly water stable metal-organic framework: Long term stability analysis in aqueous media. *Appl. Surf. Sci.* 445, 424–436. doi:10.1016/j.apsusc.2018.03.189

Mu, X., Zhang, H., Zhang, C., Yang, S., Xu, J., Huang, Y., et al. (2021). Poly (vinylidene fluoride-trifluoroethylene)/cobalt ferrite composite films with a self-biased magnetoelectric effect for flexible AC magnetic sensors. *J. Mater. Sci.* 56, 9728–9740. doi:10.1007/s10853-021-05937-8

Mukherjee, D., Van der Bruggestn, B., and Mandal, B. (2022). Advancements in visible light responsive MOF composites for photocatalytic decontamination of textile wastewater: A review. *Chemosphere* 295, 133835. doi:10.1016/j.chemosphere.2022.133835

Nidheesh, P. V., Gandhimathi, R., and Ramesh, S. T. (2013). Degradation of dyes from aqueous solution by fenton processes: A review. *Environ. Sci. Pollut. Res.* 20, 2099–2132. doi:10.1007/s11356-012-1385-z

Ning, X., Wu, Y., Ma, X., Zhang, Z., Gao, R., Chen, J., et al. (2019). A novel charge transfer channel to simultaneously enhance photocatalytic water splitting activity and stability of CdS. *Adv. Funct. Mater.* 29, 1902992. doi:10.1002/adfm.201902992

Pan, B., Wu, Y., Rhimi, B., Qin, J., Huang, Y., Yuan, M., et al. (2021). Oxygen-doping of ZnIn2S4 nanosheets towards boosted photocatalytic CO2 reduction. *J. Energy Chem.* 57, 1–9. doi:10.1016/j.jechem.2020.08.024

Pan, B., Zhou, L., Qin, J., Liao, M., and Wang, C. (2022). Modulating CoFeOX nanosheets towards enhanced CO2 photoreduction to syngas: Effect of calcination temperature and mixed-valence multi-metals. *Chemistry–A Eur. J.* 2022, e202201992. doi:10.1002/chem.202201992

Qi, P., Luo, R., Pichler, T., Zeng, J., Wang, Y., Fan, Y., et al. (2019). Development of a magnetic core-shell Fe3O4@ TA@ UiO-66 microsphere for removal of arsenic (III) and antimony (III) from aqueous solution. *J. Hazard. Mater.* 378, 120721. doi:10.1016/j.jhazmat.2019.05.114

Qin, L., Wang, R., Xin, X., Zhang, M., Liu, T., Lv, H., et al. (2022). A dual-functional supramolecular assembly for enhanced photocatalytic hydrogen evolution. *Appl. Catal. B Environ.* 312, 121386. doi:10.1016/j.apcatb.2022.121386

Qin, Y., Hao, M., and Li, Z. (2020). Metal–organic frameworks for photocatalysis. *Interface Sci. Technol.* 31, 541–579. doi:10.1016/B978-0-08-102890-2.00017-8

Qiu, J., Zhang, X., Xie, K., Zhang, X.-F., Feng, Y., Jia, M., et al. (2019). Noble metal nanoparticle-functionalized Zr-metal organic frameworks with excellent photocatalytic performance. *J. colloid interface Sci.* 538, 569–577. doi:10.1016/j.jcis.2018.12.024

Quach, T.-A., Becerra, J., Nguyen, D.-T., Sakar, M., Vu, M.-H., Dion, F., et al. (2022). Direct Z-scheme mediated SmVO4/UiO-66-NH2 heterojunction nanocomposite for the degradation of antibiotic tetracycline hydrochloride molecules under sunlight. *Chemosphere* 303, 134861. doi:10.1016/j.chemosphere.2022.134861

Ramos, M., Santana, C., Velloso, C., Da Silva, A., Magalhães, F., and Aguiar, A. (2021). A review on the treatment of textile industry effluents through Fenton processes. *Process Saf. Environ. Prot.* 155, 366–386. doi:10.1016/j.psep.2021.09.029

Salunkhe, R. R., Tang, J., Kamachi, Y., Nakato, T., Kim, J. H., and Yamauchi, Y. (2015). Asymmetric supercapacitors using 3D nanoporous carbon and cobalt oxide electrodes synthesized from a single metal–organic framework. *ACS Nano* 9, 6288–6296. doi:10.1021/acsnano.5b01790

Shahjuee, T., Masoudpanah, S. M., and Mirkazemi, S. M. (2017). Coprecipitation synthesis of CoFe2O4 nanoparticles for hyperthermia. *J. Ultrafine Grained Nanostructured Mater.* 50, 105–110.

Shangkum, G. Y., Chammingkwan, P., Trinh, D. X., and Taniike, T. (2018). Design of a semi-continuous selective layer based on deposition of UiO-66 nanoparticles for nanofiltration. *Membranes* 8, 129. doi:10.3390/membranes8040129

Shawky, A., and Alshaikh, H. (2022). Cobalt ferrite-modified sol-gel synthesized ZnO nanoplatelets for fast and bearable visible light remediation of ciprofloxacin in water. *Environ. Res.* 205, 112462. doi:10.1016/j.envres.2021.112462

Shen, L., Liang, R., Luo, M., Jing, F., and Wu, L. (2015a). Electronic effects of ligand substitution on metal–organic framework photocatalysts: The case study of UiO-66. *Phys. Chem. Chem. Phys.* 17, 117–121. doi:10.1039/c4cp04162c

Shen, L., Luo, M., Liu, Y., Liang, R., Jing, F., and Wu, L. (2015b). Noble-metal-free MoS2 co-catalyst decorated UiO-66/CdS hybrids for efficient photocatalytic H2 production. *Appl. Catal. B Environ.* 166, 445–453. doi:10.1016/j.apcatb.2014.11.056

Shi, L., Zou, X., Wang, T., Wang, D., Fan, M., and Gong, Z. (2022). Sunlight photocatalytic degradation of ofloxacin using UiO-66/wood composite photocatalysts. *Chin. Chem. Lett.* 33, 442–446. doi:10.1016/j.cclet.2021.06.048

Sivula, K. (2020). Are organic semiconductors viable for robust, high-efficiency artificial photosynthesis? *ACS Energy Lett.* 5, 1970–1973. doi:10.1021/acsenergylett.0c01084

Sohrabnezhad, S., and Moghadamy, S. (2022). Zinc oxide nanorods incorporated magnetic isoreticular metal–organic framework for photodegradation of dyes. *J. Mol. Struct.* 1247, 131353. doi:10.1016/j.molstruc.2021.131353

Subhan, S., Yaseen, M., Ahmad, B., Tong, Z., Subhan, F., Ahmad, W., et al. (2021). Fabrication of MnO2 NPs incorporated UiO-66 for the green and efficient oxidative desulfurization and denitrogenation of fuel oils. *J. Environ. Chem. Eng.* 9, 105179. doi:10.1016/j.jece.2021.105179

Subudhi, S., Paramanik, L., Sultana, S., Mansingh, S., Mohapatra, P., and Parida, K. (2020). A type-II interband alignment heterojunction architecture of cobalt titanate integrated UiO-66-NH2: A visible light mediated photocatalytic approach directed towards norfloxacin degradation and green energy (hydrogen) evolution. *J. Colloid Interface Sci.* 568, 89–105. doi:10.1016/j.jcis.2020.02.043

Taddei, M., Schukraft, G. M., Warwick, M. E., Tiana, D., McPherson, M. J., Jones, D. R., et al. (2019). Band gap modulation in zirconium-based metal–organic frameworks by defect engineering. *J. Mater. Chem. A* 7, 23781–23786. doi:10.1039/c9ta05216j

Wang, A., Zhou, Y., Wang, Z., Chen, M., Sun, L., and Liu, X. (2016). Titanium incorporated with UiO-66 (Zr)-type metal–organic framework (MOF) for photocatalytic application. *RSC Adv.* 6, 3671–3679. doi:10.1039/c5ra24135a

Wang, C., Li, A.-R., and Ma, Y.-L. (2021a). Phosphomolybdic acid niched in the metal-organic framework UiO-66 with defects: An efficient and stable catalyst for oxidative desulfurization. *Fuel Process. Technol.* 212, 106629. doi:10.1016/j.fuproc.2020.106629

Wang, J., Yuan, M., Li, C., Zhang, B., Zhu, J., Hao, X., et al. (2022). One-Step construction of polyimide/NH2-UiO-66 heterojunction for enhanced photocatalytic degradation of sulfonamides. *J. Colloid Interface Sci.* 612, 536–549. doi:10.1016/j.jcis.2021.12.190

Wang, P., Sun, L., Ye, J., Liu, Q., Fei, Z., Chen, X., et al. (2021b). Construction of crystal defect sites in UiO-66 for adsorption of dimethyl phthalate and phthalic acid. *Microporous Mesoporous Mater.* 312, 110778. doi:10.1016/j.micromeso.2020.110778

Wang, Y., Jin, H., Ma, Q., Mo, K., Mao, H., Feldhoff, A., et al. (2020a). A MOF glass membrane for gas separation. *Angew. Chem.* 132, 4395–4399. doi:10.1002/ange.201915807

Wang, Y., Yan, J., Wen, N., Xiong, H., Cai, S., He, Q., et al. (2020b). Metal-organic frameworks for stimuli-responsive drug delivery. *Biomaterials* 230, 119619. doi:10.1016/j.biomaterials.2019.119619

Wang, Y., Zhang, S., Zhao, Y., Bedia, J., Rodriguez, J., and Belver, C. (2021c). UiO-66-based metal organic frameworks for the photodegradation of acetaminophen under simulated solar irradiation. *J. Environ. Chem. Eng.* 9, 106087. doi:10.1016/j.jece.2021.106087

Wang, Z., Jiang, L., Wang, K., Li, Y., and Zhang, G. (2021d). Novel AgI/BiSbO4 heterojunction for efficient photocatalytic degradation of organic pollutants under visible light: Interfacial electron transfer pathway, DFT calculation and degradation mechanism study. *J. Hazard. Mater.* 410, 124948. doi:10.1016/j.jhazmat.2020.124948

Wei, F., Wang, H., Ran, W., Liu, T., and Liu, X. (2019). Preparation of S–N co-doped CoFe 2 O 4@ rGO@ TiO 2 nanoparticles and their superior UV-Vis light photocatalytic activities. *RSC Adv.* 9, 6152–6162. doi:10.1039/c8ra10238d

Wei, Q., Xiong, S., Li, W., Jin, C., Chen, Y., Hou, L., et al. (2021). Double Z-scheme system of α-SnWO4/UiO-66 (NH2)/g-C3N4 ternary heterojunction with enhanced photocatalytic performance for ibuprofen degradation and H2 evolution. *J. Alloys Compd.* 885, 160984. doi:10.1016/j.jallcom.2021.160984

Wen, M., Li, G., Liu, H., Chen, J., An, T., and Yamashita, H. (2019). Metal–organic framework-based nanomaterials for adsorption and photocatalytic degradation of gaseous pollutants: Recent progress and challenges. *Environ. Sci. Nano* 6, 1006–1025. doi:10.1039/c8en01167b

Winarta, J., Shan, B., Mcintyre, S. M., Ye, L., Wang, C., Liu, J., et al. (2019). A decade of UiO-66 research: A historic review of dynamic structure, synthesis mechanisms, and characterization techniques of an archetypal metal–organic framework. *Cryst. Growth & Des.* 20, 1347–1362. doi:10.1021/acs.cgd.9b00955

Xia, T., Lin, Y., Li, W., and Ju, M. (2021). Photocatalytic degradation of organic pollutants by MOFs based materials: A review. *Chin. Chem. Lett.* 32, 2975–2984. doi:10.1016/j.cclet.2021.02.058

Xiong, L., and Tang, J. (2021). Strategies and challenges on selectivity of photocatalytic oxidation of organic substances. *Adv. Energy Mater.* 11, 2003216. doi:10.1002/aenm.202003216

Xiong, X., Zhao, Y., Shi, R., Yin, W., Zhao, Y., Waterhouse, G. I., et al. (2020). Selective photocatalytic CO2 reduction over Zn-based layered double hydroxides

containing tri or tetravalent metals. *Sci. Bull.* 65, 987–994. doi:10.1016/j.scib.2020.03.032

Xu, F., Zhang, Q., An, R., Li, L., and Zhou, L. (2022). Facile fabrication of flower-like NH2-UIO-66/BiOCl Z-scheme heterojunctions with largely improved photocatalytic performance for removal of tetracycline under solar irradiation. *J. Alloys Compd.* 899, 163324. doi:10.1016/j.jallcom.2021.163324

Xu, J., Varghese, J., Portale, G., Longo, A., Momand, J., Syari'ati, A., et al. (2019). Chemical solution deposition of ordered 2D arrays of room-temperature ferrimagnetic cobalt ferrite nanodots. *Polymers* 11, 1598. doi:10.3390/polym11101598

Xu, X., Liu, R., Cui, Y., Liang, X., Lei, C., Meng, S., et al. (2017). PANI/FeUiO-66 nanohybrids with enhanced visible-light promoted photocatalytic activity for the selectively aerobic oxidation of aromatic alcohols. *Appl. Catal. B Environ.* 210, 484–494. doi:10.1016/j.apcatb.2017.04.021

Yang, Z., Tong, X., Feng, J., He, S., Fu, M., Niu, X., et al. (2019). Flower-like BiOBr/UiO-66-NH2 nanosphere with improved photocatalytic property for norfloxacin removal. *Chemosphere* 220, 98–106. doi:10.1016/j.chemosphere.2018.12.086

Yaseen, D., and Scholz, M. (2019). Textile dye wastewater characteristics and constituents of synthetic effluents: A critical review. *Int. J. Environ. Sci. Technol.* 16, 1193–1226. doi:10.1007/s13762-018-2130-z

Yassin, J. M., Taddesse, A. M., and Sánchez-Sánchez, M. (2022). Sustainable synthesis of semicrystalline Zr-BDC MOF and heterostructural Ag3PO4/Zr-BDC/g-C3N4 composite for photocatalytic dye degradation. *Catal. Today* 390, 162–175. doi:10.1016/j.cattod.2021.11.037

Yavari, S., Mahmodi, N. M., Teymouri, P., Shahmoradi, B., and Maleki, A. (2016). Cobalt ferrite nanoparticles: Preparation, characterization and anionic dye removal capability. *J. Taiwan Inst. Chem. Eng.* 59, 320–329. doi:10.1016/j.jtice.2015.08.011

Yi, X.-H., Ma, S.-Q., Du, X.-D., Zhao, C., Fu, H., Wang, P., et al. (2019). The facile fabrication of 2D/3D Z-scheme g-C3N4/UiO-66 heterojunction with enhanced photocatalytic Cr (VI) reduction performance under white light. *Chem. Eng. J.* 375, 121944. doi:10.1016/j.cej.2019.121944

Younes, H. A., Taha, M., Mahmoud, R., Mahmoud, H. M., and Abdelhameed, R. M. (2022). High adsorption of sodium diclofenac on post-synthetic modified zirconium-based metal-organic frameworks: Experimental and theoretical studies. *J. Colloid Interface Sci.* 607, 334–346. doi:10.1016/j.jcis.2021.08.158

Yuan, N., Gong, X., Sun, W., and Yu, C. (2021). Advanced applications of Zr-based MOFs in the removal of water pollutants. *Chemosphere* 267, 128863. doi:10.1016/j.chemosphere.2020.128863

Yuan, S., Feng, L., Wang, K., Pang, J., Bosch, M., Lollar, C., et al. (2018). Stable metal-organic frameworks: Stable metal-organic frameworks: Design, synthesis, and applications (adv. Mater. 37/2018). *Adv. Mater.* 30, 1870277. doi:10.1002/adma.201870277

Zeng, Y., Guo, N., Song, Y., Zhao, Y., Li, H., Xu, X., et al. (2018). Fabrication of Z-scheme magnetic MoS2/CoFe2O4 nanocomposites with highly efficient photocatalytic activity. *J. colloid interface Sci.* 514, 664–674. doi:10.1016/j.jcis.2017.12.079

Zhang, A., Liu, B., Liu, M., Xie, Z., Wang, D., and Feng, G. (2021a). The adsorption properties of defect controlled metal-organic frameworks of UiO-66. *Sep. Purif. Technol.* 270, 118842. doi:10.1016/j.seppur.2021.118842

Zhang, F., Cheng, W., Yu, Z., Ge, S., Shao, Q., Pan, D., et al. (2021b). Microwave hydrothermally synthesized WO3/UiO-66 nanocomposites toward enhanced photocatalytic degradation of rhodamine B. *Adv. Compos. Hybrid Mater.* 4, 1330–1342. doi:10.1007/s42114-021-00346-6

Zhang, G., Jin, L., Zhang, R., Bai, Y., Zhu, R., and Pang, H. (2021c). Recent advances in the development of electronically and ionically conductive metal-organic frameworks. *Coord. Chem. Rev.* 439, 213915. doi:10.1016/j.ccr.2021.213915

Zhang, L., Li, P., Feng, L., Chen, X., Jiang, J., Zhang, S., et al. (2020). Controllable fabrication of visible-light-driven CoSx/CdS photocatalysts with direct Z-scheme heterojunctions for photocatalytic Cr (VI) reduction with high efficiency. *Chem. Eng. J.* 397, 125464. doi:10.1016/j.cej.2020.125464

Zhang, R., Du, B., Li, Q., Cao, Z., Feng, G., and Wang, X. (2019a). α-Fe2O3 nanoclusters confined into UiO-66 for efficient visible-light photodegradation performance. *Appl. Surf. Sci.* 466, 956–963. doi:10.1016/j.apsusc.2018.10.048

Zhang, S., Zhao, Y., Shi, R., Waterhouse, G. I., and Zhang, T. (2019b). Photocatalytic ammonia synthesis: Recent progress and future. *EnergyChem* 1, 100013. doi:10.1016/j.enchem.2019.100013

Zhang, X., Tong, S., Huang, D., Liu, Z., Shao, B., Liang, Q., et al. (2021d). Recent advances of Zr based metal organic frameworks photocatalysis: Energy production and environmental remediation. *Coord. Chem. Rev.* 448, 214177. doi:10.1016/j.ccr.2021.214177

Zhang, X., Yang, Y., Lv, X., Wang, Y., Liu, N., Chen, D., et al. (2019c). Adsorption/desorption kinetics and breakthrough of gaseous toluene for modified microporous-mesoporous UiO-66 metal organic framework. *J. Hazard. Mater.* 366, 140–150. doi:10.1016/j.jhazmat.2018.11.099

Zhang, Y.-P., Han, W., Yang, Y., Zhang, H.-Y., Wang, Y., Wang, L., et al. (2022). S-scheme heterojunction of black TiO2 and covalent-organic framework for enhanced photocatalytic hydrogen evolution. *Chem. Eng. J.* 446, 137213. doi:10.1016/j.cej.2022.137213

Zhang, Y., Zhou, J., Feng, Q., Chen, X., and Hu, Z. (2018). Visible light photocatalytic degradation of MB using UiO-66/g-C3N4 heterojunction nanocatalyst. *Chemosphere* 212, 523–532. doi:10.1016/j.chemosphere.2018.08.117

Zhao, H., Liu, X., Dong, Y., Xia, Y., and Wang, H. (2019). A special synthesis of BiOCl photocatalyst for efficient pollutants removal: New insight into the band structure regulation and molecular oxygen activation. *Appl. Catal. B Environ.* 256, 117872. doi:10.1016/j.apcatb.2019.117872

Zhou, C., Lai, C., Huang, D., Zeng, G., Zhang, C., Cheng, M., et al. (2018). Highly porous carbon nitride by supramolecular preassembly of monomers for photocatalytic removal of sulfamethazine under visible light driven. *Appl. Catal. B Environ.* 220, 202–210. doi:10.1016/j.apcatb.2017.08.055

Zhou, C., Xia, W., Huang, D., Cheng, M., Zhang, H., Cai, T., et al. (2021). Strategies for enhancing the perylene diimide photocatalytic degradation activity: Method, effect factor, and mechanism. *Environ. Sci. Nano* 8, 602–618. doi:10.1039/d0en01245a

Zhou, G., Fu, Y., Zhou, R., Zhang, L., Zhang, L., Deng, J., et al. (2022). Efficient degradation of organic contaminants by magnetic cobalt ferrite combined with peracetic acid. *Process Saf. Environ. Prot.* 160, 376. doi:10.1016/j.psep.2022.02.031

Zhou, L., Ji, L., Ma, P.-C., Shao, Y., Zhang, H., Gao, W., et al. (2014). Development of carbon nanotubes/CoFe2O4 magnetic hybrid material for removal of tetrabromobisphenol A and Pb (II). *J. Hazard. Mater.* 265, 104–114. doi:10.1016/j.jhazmat.2013.11.058

Zou, X., Zhao, X., Zhang, J., Lv, W., Qiu, L., and Zhang, Z. (2021). Photocatalytic degradation of ranitidine and reduction of nitrosamine dimethylamine formation potential over MXene–Ti3C2/MoS2 under visible light irradiation. *J. Hazard. Mater.* 413, 125424. doi:10.1016/j.jhazmat.2021.125424